A&A 587, A56 (2016)
DOI: 10.1051/0004-6361/201526594


Astronomy & Astrophysics

# First light of the VLT planet finder SPHERE

## II. The physical properties and the architecture of the young systems PZ Telescopii and HD 1160 revisited⋆

A.-L. Maire[1], M. Bonnefoy[2,3], C. Ginski[4], A. Vigan[5,6], S. Messina[7], D. Mesa[1], R. Galicher[8], R. Gratton[1], S. Desidera[1], T. G. Kopytova[9,10], M. Millward[11], C. Thalmann[12], R. U. Claudi[1], D. Ehrenreich[13], A. Zurlo[5,1,14,15], G. Chauvin[2,3], J. Antichi[16], A. Baruffolo[1], A. Bazzon[12], J.-L. Beuzit[2,3], P. Blanchard[5], A. Boccaletti[8], J. de Boer[6], M. Carle[5], E. Cascone[17], A. Costille[5], V. De Caprio[17], A. Delboulbé[2,3], K. Dohlen[5], C. Dominik[18], M. Feldt[9], T. Fusco[19,5], J. H. Girard[6,2,3], E. Giro[1], D. Gisler[20], L. Gluck[2,3], C. Gry[5], T. Henning[9], N. Hubin[21], E. Hugot[5], M. Jaquet[5], M. Kasper[21,2,3], A.-M. Lagrange[2,3], M. Langlois[22,5], D. Le Mignant[5], M. Llored[5], F. Madec[5], P. Martinez[23], D. Mawet[24], J. Milli[6,2,3], O. Möller-Nilsson[9], D. Mouillet[2,3], T. Moulin[2,3], C. Moutou[5,25], A. Origné[5], A. Pavlov[9], C. Petit[19], J. Pragt[26], P. Puget[2,3], J. Ramos[9], S. Rochat[2,3], R. Roelfsema[26], B. Salasnich[1], J.-F. Sauvage[19,5], H. M. Schmid[12], M. Turatto[1], S. Udry[13], F. Vakili[23], Z. Wahhaj[6,5], L. Weber[13], and F. Wildi[13]

*(Affiliations can be found after the references)*

Received 25 May 2015 / Accepted 13 October 2015

**ABSTRACT**

*Context.* The young systems PZ Tel and HD 1160, hosting known low-mass companions, were observed during the commissioning of the new planet finder of the Very Large Telescope (VLT) SPHERE with several imaging and spectroscopic modes.
*Aims.* We aim to refine the physical properties and architecture of both systems.
*Methods.* We use SPHERE commissioning data and dedicated Rapid Eye Mount (REM) observations, as well as literature and unpublished data from VLT/SINFONI, VLT/NaCo, Gemini/NICI, and Keck/NIRC2.
*Results.* We derive new photometry and confirm the short-term ($P$ = 0.94 d) photometric variability of the star PZ Tel A with values of 0.14 and 0.06 mag at optical and near-infrared wavelengths, respectively. We note from the comparison to literature data spanning 38 yr that the star also exhibits a long-term variability trend with a brightening of ∼0.25 mag. The 0.63−3.8 $\mu$m spectral energy distribution of PZ Tel B (separation ∼25 AU) allows us to revise its physical characteristics: spectral type M7 ± 1, $T_{\rm eff}$ = 2700 ± 100 K, log($g$) < 4.5 dex, luminosity log($L/L_{\odot}$) = −2.51 ± 0.10 dex, and mass 38−72 $M_{\rm J}$ from "hot-start" evolutionary models combining the ranges of the temperature and luminosity estimates. The 1−3.8 $\mu$m SED of HD 1160 B (∼85 au) suggests a massive brown dwarf or a low-mass star with spectral type M6.0$^{+1.0}_{-0.5}$, $T_{\rm eff}$ = 3000 ± 100 K, subsolar metallicity [M/H] = −0.5−0.0 dex, luminosity log($L/L_{\odot}$) = −2.81 ± 0.10 dex, and mass 39−166 $M_{\rm J}$. The physical properties derived for HD 1160 C (∼560 au) from $K_{\rm s}L'$-band photometry are consistent with the discovery study. The orbital study of PZ Tel B confirms its deceleration and the high eccentricity of its orbit ($e$ > 0.66). For eccentricities below 0.9, the inclination, longitude of the ascending node, and time of periastron passage are well constrained. In particular, both star and companion inclinations are compatible with a system seen edge-on. Based on "hot-start" evolutionary models, we reject other brown dwarf candidates outside 0.25″ for both systems, and giant planet companions outside 0.5″ that are more massive than 3 $M_{\rm J}$ for the PZ Tel system. We also show that $K1 - K2$ color can be used along with $YJH$ low-resolution spectra to identify young L-type companions, provided high photometric accuracy (≤0.05 mag) is achieved.
*Conclusions.* SPHERE opens new horizons in the study of young brown dwarfs and giant exoplanets using direct imaging thanks to high-contrast imaging capabilities at optical (0.5−0.9 $\mu$m) and near-infrared (0.95−2.3 $\mu$m) wavelengths, as well as high signal-to-noise spectroscopy in the near-infrared domain (0.95−2.3 $\mu$m) from low resolutions ($R$ ∼ 30−50) to medium resolutions ($R$ ∼ 350).

**Key words.** brown dwarfs – stars: individual: PZ Telescopii – stars: individual: HD 1160 – techniques: high angular resolution – techniques: image processing – techniques: spectroscopic

## 1. Introduction

Direct imaging of young (≲300 Myr) stars has revealed a population of giant planet and brown dwarf companions at wide (>5 au) separations (e.g., Chauvin et al. 2005a,b; Itoh et al. 2005; Luhman et al. 2006, 2007; Marois et al. 2008, 2010b; Thalmann et al. 2009; Lagrange et al. 2010; Biller et al. 2010; Mugrauer et al. 2010; Lafrenière et al. 2010; Carson et al. 2013; Kuzuhara et al. 2013; Rameau et al. 2013a; Bailey et al. 2014). Several formation mechanisms have been proposed to account for the diversity of these objects: core accretion (Pollack et al. 1996), gravitational instability (Boss 1997), and binary-like formation. Direct imaging surveys attempted to place first constraints on the occurrence of giant planets (∼10−20%) and/or brown dwarfs (∼1−3%) and their formation mechanisms for separations beyond ∼10−20 au (e.g., Lafrenière et al. 2007; Chauvin et al. 2010, 2015; Ehrenreich et al. 2010; Vigan et al. 2012b; Rameau et al. 2013b; Wahhaj et al. 2013; Nielsen et al. 2013; Biller et al. 2013; Brandt et al. 2014). A new generation of high-contrast imaging instruments designed to search for and characterize giant exoplanets at separations as close as

⋆ Based on data collected at the European Southern Observatory, Chile, during the commissioning of the SPHERE instrument and ESO programs 085.C-0277, 087.C-0109, 087.C-0535, and 060.A-9026.

the snow line (~5 au), such as the Spectro-Polarimetric High-contrast Exoplanet REsearch (SPHERE, Beuzit et al. 2008) and the Gemini Planet Imager (GPI, Macintosh et al. 2014), have recently started operations.

We present in this paper SPHERE first light observations of the young systems PZ Tel (Biller et al. 2010; Mugrauer et al. 2010) and HD 1160 (Nielsen et al. 2012). This includes near-infrared images and integral field spectroscopy at low resolution ($R \sim 30$) for the brown dwarf companions PZ Tel B and HD 1160 B, as well as optical images and near-infrared long-slit spectroscopy at low and medium resolutions ($R \sim 50$ and 350) for PZ Tel B.

PZ Tel is a G9IV star (Torres et al. 2006) member of the young ($21 \pm 4$ Myr, Binks & Jeffries 2014) stellar association $\beta$ Pictoris (Zuckerman et al. 2001; Torres et al. 2008) and located at a distance $d = 51.5 \pm 2.6$ pc (van Leeuwen 2007). The host star was first known to be single (Balona 1987; Innis et al. 1988) and to show activity-related to starspots with a rotational period of 0.94486 d (Coates et al. 1980) and lightcurve amplitude variations up to $\Delta V = 0.22$ mag (Innis et al. 1990). A late-M brown dwarf companion to PZ Tel was discovered independently by two teams (Biller et al. 2010; Mugrauer et al. 2010). Using Gemini/NICI photometry in the $J$, $H$, and $K_s$ bands, Biller et al. (2010) estimate a spectral type of M5−M9, an effective temperature of $T_{\rm eff} = 2700 \pm 84$ K, and a surface gravity of $\log(g) = 4.20 \pm 0.11$ dex. Mugrauer et al. (2010) derive photometry in the same bands from VLT/NaCo data and find a spectral type and an effective temperature consistent with the results of Biller et al. (2010): M6−M8 and 2500−2700 K, respectively.

Astrometric follow-up of the companion shows significant orbital motion (separation increase of ~35 mas/yr) and suggests that its orbit is highly eccentric (>0.6, Biller et al. 2010; Mugrauer et al. 2012; Ginski et al. 2014). Mugrauer et al. (2012) detect a deceleration of the companion using NaCo data taken in 2007 and 2009, suggesting that the companion gets closer to its apoastron. Ginski et al. (2014) note a similar trend using 2012 NaCo data, although at low significance ($\sim 2\sigma$), and advocate for further astrometric monitoring. Near-infrared (NIR) spectroscopic observations with VLT/SINFONI in the $H + K$ bands at medium resolution ($R = 1500$) of the host star and the companion indicate spectral types of G6.5 and M6−L0, respectively (Schmidt et al. 2014). Schmidt et al. (2014) also derive for the companion $T_{\rm eff} = 2500^{+138}_{-115}$ K, $\log(g) = 3.5^{+0.51}_{-0.30}$ dex, a metallicity enhancement $[{\rm M/H}] = 0.30^{+0.00}_{-0.30}$ dex, a radius $R = 2.42^{+0.28}_{-0.34}\ R_{\rm J}$ (Jupiter radii), and a range for the mass $M = 3.2$−$24.4\ M_{\rm J}$ (Jupiter masses) with a most likely value of 21 $M_{\rm J}$. Schmidt et al. (2014) stress the need for spectra of PZ Tel B with better quality and wider coverage to further constrain its physical properties. Using HARPS, Lagrange et al. (2013) measure for PZ Tel A a projected rotational velocity $v \sin(i) = 80$ km s$^{-1}$, but the short time baseline and the small amplitude of the radial velocity variations prevent a trend due to PZ Tel B. Rebull et al. (2008) find an excess at 70 $\mu$m using *Spitzer*/MIPS but not at 24 $\mu$m. Rebull et al. (2008) attribute the 70-$\mu$m excess to a low-mass (~0.3 lunar masses) and cold ($T_{\rm eff} \sim 41$ K) debris disk spanning a range of separations 35−165 au. However, this hypothesis is rejected by Biller et al. (2013), because of a likely wrong star identification in the *Spitzer* data, and Riviere-Marichalar et al. (2014), who find no IR excesses with *Herschel*/PACS at 70, 100, and 160 $\mu$m.

HD 1160 is a moderately young ($50^{+50}_{-40}$ Myr) A0V star located at a distance $d = 108.5 \pm 5.0$ pc (van Leeuwen 2007), which is not classified as a member of any of the known young stellar associations (Nielsen et al. 2012). This star hosts two low-mass companions at projected separations ~85 and ~560 au (Nielsen et al. 2012) discovered as part of the Gemini NICI Planet-Finding Campaign (Liu et al. 2010b). Nielsen et al. (2012) show that both companions are gravitationally bound using archival data from VLT/NaCo and VLT/ISAAC spanning almost a decade (2002−2011) and obtained for purposes of photometric calibration. They also present Gemini/NICI photometry in the $J$, $H$, and $K_s$ bands and Keck/NIRC2 photometry in the $L'$ and $M_s$ bands for both companions and NIR IRTF/SpeX spectra for the farthest companion. Using the NICI photometry, these authors find that both companions have colors at odds with field M dwarfs but consistent with colors of giant M stars, although the companions cannot be giant stars based on their absolute magnitude. Nielsen et al. (2012) are not able to explain this discrepancy, but note that an error in the calibration of the NICI photometry could account for it. For HD 1160 C, the spectrum indicates a low-mass star of spectral type M3.5 ± 0.5 and mass $M = 0.22^{+0.03}_{-0.04}$ solar masses ($M_\odot$). For HD 1160 B, the photometry suggests a brown dwarf of spectral type L0 ± 2 and mass $M = 33^{+12}_{-9}\ M_{\rm J}$. Bonnefoy et al. (2014b) argue that HD 1160 B may have formed according to the gravitational instability scenario (Boss 1997) in a massive disk (~20% of the host star mass).

We describe the observations and the data reduction in Sects. 2 and 3. Then we present new analyses of the physical properties of PZ Tel A (Sect. 4), the spectral energy distribution (SED) of the companions for both systems (Sect. 5), the orbit of PZ Tel B (Sect. 6), as well as further constraints on putative additional companions in each system (Sect. 7).

## 2. Observations

The SPHERE planet-finder instrument installed at the VLT (Beuzit et al. 2008) is a highly specialized instrument dedicated to high-contrast imaging and the spectroscopy of young giant exoplanet. It was built by a large consortium of European institutes and is based on the SAXO system (Sphere Adaptive Optics for eXoplanet Observation, Fusco et al. 2006, 2014; Petit et al. 2014; Sauvage et al. 2014), which includes a 41 × 41-actuator wavefront control, pupil stabilization, differential tip tilt control and stress polished toric mirrors (Hugot et al. 2012) for beam transportation to the coronagraphs and science subsystems. Several coronagraphs for stellar diffraction suppression are provided, including apodized pupil Lyot coronagraphs (Soummer 2005) and achromatic four-quadrant phase masks (Boccaletti et al. 2008). The instrument is equipped with three science channels: an infrared dual-band imager and spectrograph (IRDIS, Dohlen et al. 2008), an integral field spectrometer (IFS, Claudi et al. 2008), and a rapid-switching imaging polarimeter (ZIMPOL, Thalmann et al. 2008). We refer to Beuzit et al. (in prep.) for detailed descriptions of the subsystems and observing modes.

We observed PZ Tel and HD 1160 during six nights of the SPHERE commissioning runs (Table 1). The observations of PZ Tel include all the three science subsystems: IRDIS in both dual-band imaging mode (Vigan et al. 2010) and long-slit spectroscopy mode (Vigan et al. 2008), IFS, and ZIMPOL in dual-band imaging mode. HD 1160 was observed with IRDIS in dual-band imaging mode and IFS in parallel.

### 2.1. Simultaneous IRDIS and IFS observations

The observations with IRDIS in dual-band imaging mode and IFS are simultaneous (IRDIFS and IRDIFS_EXT modes in Table 1). In the IRDIFS mode, IRDIS is operated in the filter pair $H23$ (Table 2) and IFS in the bands $YJ$ (0.95−1.35 $\mu$m,

**Table 1.** Log of the SPHERE observations.

| Object | UT date | Seeing (″) | Mode | Bands | DIT (s) × NDIT | | $N_{exp}$ | ΔPA (°) |
|---|---|---|---|---|---|---|---|---|
| | | | | | IRDIS or ZIMPOL | IFS | | |
| PZ Tel | 2014/07/15 | 0.88−1.11 | IRDIFS | $H2H3{+}YJ$ | 20 × 6 | 60 × 2 | 16 | 7.6 |
| PZ Tel | 2014/08/06 | 0.5−0.7 | IRDIS-LRS | $YJHK_s$ | 20 × 10 | – | 6 | – |
| PZ Tel | 2014/08/06 | 0.6−0.7 | IRDIS-MRS | $YJH$ | 30 × 5 | – | 6 | – |
| PZ Tel | 2014/08/08 | 0.78−1.05 | IRDIFS_EXT | $K1K2{+}YJH$ | 12 × 5 | 30 × 2 | 16 | 9.0 |
| PZ Tel | 2014/08/16 | 1.12−1.58 | ZIMPOL | $R'I'$ | 50 × 12 | – | 3 | 14.1 |
| PZ Tel | 2014/10/11 | 1.12−1.97 | IRDIFS | $H2H3{+}YJ$ | 8 × 1[a] | 32 × 20[a] | 1 | 3.7[b] |
| HD 1160 | 2014/08/13 | 0.54−0.84 | IRDIFS_EXT | $K1K2{+}YJH$ | 4 × 20 | 8 × 15 | 16 | 18.4 |

**Notes.** The seeing is the value measured by the differential image motion monitor (DIMM) at 0.5 $\mu$m. DIT (detector integration time) refers to the single exposure time, NDIT (Number of Detector InTegrations) to the number of frames in a single data cube, $N_{exp}$ to the number of data cubes, and ΔPA to the amplitude of the parallactic rotation. [(a)] This sequence was a test and we only used the coronagraphic images with the satellite spots for measuring the astrometry of the companion. [(b)] For the IFS data.

**Table 2.** Photometric measurements of PZ Tel B and HD 1160 BC relative to the host star.

| Filter | $\lambda$ ($\mu$m) | $\Delta\lambda^a$ ($\mu$m) | PZ Tel B | HD 1160 B | HD 1160 C |
|---|---|---|---|---|---|
| | | | SPHERE | | |
| $R'$ | 0.6263 | 0.1486 | $9.76^{+0.22}_{-0.30}$ | – | – |
| $I'$ | 0.7897 | 0.1525 | $7.529 \pm 0.108$ | – | – |
| $H2$ | 1.5888 | 0.0531 | $5.34 \pm 0.18$ | – | – |
| $H3$ | 1.6671 | 0.0556 | $5.28 \pm 0.18$ | – | – |
| $K1$ | 2.1025 | 0.1020 | $5.29 \pm 0.08$ | $7.03 \pm 0.05$ | $5.35 \pm 0.06$ |
| $K2$ | 2.2550 | 0.1090 | $5.02 \pm 0.09$ | $6.77 \pm 0.04$ | $5.16 \pm 0.04$ |
| | | | Other instruments | | |
| $L'$ | 3.8000 | 0.6200 | $5.15 \pm 0.15^b$ | $6.54 \pm 0.10^c$ | $4.69 \pm 0.05^c$ |

**Notes.** [(a)] Full width at half maximum. [(b)] NaCo; Beust et al. (2016). [(c)] NaCo; this work.

$R \sim 54$). In the IRDIFS_EXT mode, IRDIS is operated in the filter pair $K12$ (Table 2) and IFS in the bands $YJH$ (0.95−1.65 $\mu$m, $R \sim 33$).

PZ Tel was observed twice in the IRDIFS mode and once in the IRDIFS_EXT mode. The IRDIFS sequences were obtained in poor observing conditions (July 2014) or for purposes of technical tests (October 2014). The IRDIFS_EXT sequence was acquired in better observing conditions. HD 1160 was observed in the IRDIFS_EXT mode in good observing conditions.

The sequences are obtained using the following strategy:

- The star is centered on the coronagraphic mask. The coronagraph used for all the sequences is an apodized pupil Lyot coronagraph (Soummer 2005) with inner working angle IWA ∼ 0.09″, except for the July 2014 IRDIFS sequence for which IWA ∼ 0.07″.
- A coronagraphic image with four crosswise faint replicas of the star is acquired for estimating the star location, based on the original concept proposed by Marois et al. (2006b) and Sivaramakrishnan & Oppenheimer (2006). These replicas are produced by applying a 2D periodic modulation on the deformable mirror of SPHERE. This calibration is critical for accurate registration of the frames before the application of the angular differential imaging processing (ADI, Marois et al. 2006a) and for precise relative astrometry of the detected companions.
- An unsaturated image of the star (point-spread function, PSF hereafter) is recorded for purposes of photometric calibration. This image is obtained by shifting the star out of the coronagraphic mask using a tip-tilt mirror. A neutral density filter located in the common path and infrastructure of SPHERE (so common to IRDIS and IFS) is inserted into the light beam (average transmission ∼1/100)[1].
- The science coronagraphic images are acquired in pupil-stabilized mode to take advantage of the ADI technique (Marois et al. 2006a). For IRDIS, a dither pattern of 4×4 positions with shifts of one pixel is applied to handle the detector bad pixels. For IFS, no dither pattern is used.
- A second set of a PSF and coronagraphic images with four satellite spots is recorded. This second set of calibrations allows us to evaluate the photometric error due to the stellar flux variations and the stability of the star centering.

After each sequence, six sky backgrounds are acquired, with the same exposure times used for the coronagraphic images and the PSF. All the other calibration data used in the data reduction (Sect. 3) are obtained the following day.

For calibrating the distortion, plate scale, and orientation of the IRDIS images, a field in the outer regions of the 47 Tuc globular cluster was observed during each of the observing runs with the same instrument setup (filter and coronagraph), except for the $K12$ filter pair. For the latter configuration, we used the calibration in the $H23$ filter pair. The 47 Tuc field is selected because it has a bright star for adaptive optics guiding and accurate *Hubble* Space Telescope (HST) astrometry (Bellini & Anderson, private comm.; data collected as part of the program GO-10775: P.I. Sarajedini). No IFS data of astrometric calibrators were obtained during the commissioning runs.

[1] The transmission curves of the neutral density filters can be found in the User Manual available at www.eso.org/sci/facilities/paranal/instruments/sphere/doc.html

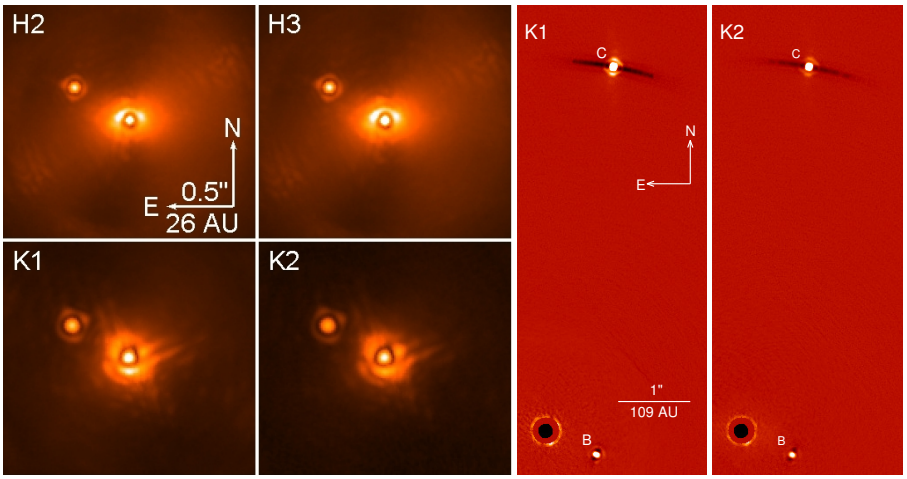


**Fig. 1.** IRDIS images of PZ Tel B in the $H23$ and $K12$ filter pairs (*left*) and HD 1160 BC in the $K12$ filter pair (*right*). The intensity scale is the same for a given target and is square root.

### 2.2. IRDIS long-slit spectroscopy

PZ Tel B was observed with the long-slit spectroscopy (LSS) mode of IRDIS with two setups (Table 1). The LSS mode includes a low-resolution mode (LRS), which covers the $YJHK_s$ bands at resolutions of 35−50 in one shot, and a medium-resolution mode (MRS), which covers the $YJH$ bands at a resolution of ∼350 (Vigan et al. 2012a). The LSS observations are always performed in field-stabilized mode to keep the object within the slit during the complete integration. A sequence consists of images with the star behind the coronagraph, an off-axis reference PSF, in which the star is shifted out of the coronagraph within the slit, and finally a series of sky backgrounds. The sky backgrounds are particularly important for the LRS mode that covers the $K_s$ band, for which the thermal background of the instrument and sky are much higher. The sequences do not differ between the LRS and MRS modes except for the change of the dispersive element. For the observations reported in this paper, we used the configuration Wide slit and Large mask (WL), where the width of the slit is 120 mas and the radius of the coronagraphic mask is 0.2″. No spectrophotometric calibrator was observed after the sequences. Other calibrations (darks, flat fields) were acquired during the morning following the observations.

### 2.3. ZIMPOL imaging

PZ Tel B was observed simultaneously in the $R'$ and $I'$ broadband filters with the two camera channels of ZIMPOL (Table 1). To implement ADI (Marois et al. 2006a), the sequence of science observations was obtained in pupil-stabilized mode. A classical Lyot coronagraph (Lyot 1932) of diameter 155 mas and the satellite spots were also used. The sequence was started about 30 min after the meridian passage of PZ Tel. For photometric calibration, the unsaturated PSF of the primary star was acquired once after the science sequence. For this purpose, a tip-tilt mirror was used to move the star away from the coronagraph. No neutral density filter was inserted into the light beam. To avoid saturation, the exposure time for the PSF was set to 2 s. A total of twenty subintegrations in one data cube were taken in this case. The companion is well detected in the raw (without any preprocessing) individual $I'$-band science images and in the preprocessed $I'$-band PSF (after cosmetic correction, frame registering, and median combination). For data reduction purposes, special domeflats with the coronagraph in place were taken right after the observations. In addition, bias frames were taken during the following day.

### 2.4. SINFONI integral field spectroscopy

For comparison purposes, we compare the SPHERE IFS and LSS spectra of PZ Tel B to archival SINFONI data. SINFONI (Eisenhauer et al. 2003; Bonnet et al. 2004) was operated with the adaptive optics system of the instrument locked on the star. The system was observed on September 5, 9, and 13, 2011 with the $J$-band and $H + K$ band grating and the preoptics leading to a 25 × 50 mas sampling of the 0.8″ × 0.8″ field of view (ESO program 087.C-0535, P.I. Tecza). Additional observations were obtained in the $H + K$ band on September 8, 2011. We also reanalyzed the observations made on August 22, 2011 (ESO program 087.C-0109, P.I. Mugrauer) with the $H + K$ band grating and the preoptics leading to 25 × 50 mas spaxels and presented by Schmidt et al. (2014). With respect to the spectra presented in Schmidt et al. (2014), the combined SINFONI observations enabled us to extend the wavelength coverage to the $J$ band and to improve the signal-to-noise ratio (S/N) in the $H$ band from 5 to 10 (no S/N improvement in the $K$ band, $S/N = 11$).

## 3. Data reduction and analysis

### 3.1. IRDIS imaging

All the data reported in Table 1 were preprocessed in the same way: subtraction of the sky background, correction of the flat field, processing of the bad pixels, and registration of the frames using the coronagraphic images with the satellite spots. Then the data were processed using derotation and median-stacking of the temporal frames in each filter separately in the case of the PZ Tel data sets (Fig. 1, left) and differential imaging for the HD 1160 data set. For the PZ Tel data sets, we checked that the derived photometric values agree with the photometry extracted using the TLOCI differential imaging algorithm (see below).

In the second case, two independent algorithms were considered for calibrating the stellar residuals. The main algorithm was an upgrade of the Template Locally Optimized Combination of Images algorithm (TLOCI, Marois et al. 2014). A second algorithm, which was used for checks for the photometry of the companions and provided consistent results within the error bars

**Table 3.** Astrometric measurements of PZ Tel B and HD 1160 BC relative to the host star.

| Object | Instrument | Epoch | Band | Separation (mas) | Parallactic angle (°) |
|---|---|---|---|---|---|
| PZ Tel B | IFS | 2014.53 | $YJ$ | $478.22 \pm 0.70$ | $59.71 \pm 0.19$ |
| PZ Tel B | IFS | 2014.60 | $YJH$ | $479.53 \pm 0.69$ | $59.62 \pm 0.14$ |
| PZ Tel B | IFS | 2014.78 | $YJ$ | $482.60 \pm 0.93$ | $59.44 \pm 0.15$ |
| PZ Tel B | IRDIS | 2014.53 | $H2$ | $478.48 \pm 2.10$ | $59.58 \pm 0.48$ |
| PZ Tel B | IRDIS | 2014.53 | $H3$ | $476.44 \pm 2.09$ | $60.06 \pm 0.49$ |
| PZ Tel B | IRDIS | 2014.60 | $K1$ | $479.69 \pm 0.34$ | $59.71 \pm 0.47$ |
| PZ Tel B | IRDIS | 2014.60 | $K2$ | $479.61 \pm 0.34$ | $60.17 \pm 0.47$ |
| PZ Tel B | IRDIS | 2014.78 | $H2$ | $483.87 \pm 0.34$ | $59.49 \pm 0.16$ |
| PZ Tel B | IRDIS | 2014.78 | $H3$ | $483.87 \pm 0.29$ | $59.51 \pm 0.16$ |
| HD 1160 B | IFS | 2014.62 | $YJH$ | $780.87 \pm 1.06$ | $244.25 \pm 0.13$ |
| HD 1160 B | IRDIS | 2014.62 | $K1$ | $780.97 \pm 0.47$ | $243.89 \pm 0.21$ |
| HD 1160 C | IRDIS | 2014.62 | $K1$ | $5149.75 \pm 2.69$ | $349.17 \pm 0.10$ |

**Notes.** The IFS and IRDIS measurements were obtained from the coronagraphic images with the satellite spots (Sect. 2).

with respect to the TLOCI pipeline, consisted in derotating and median-combining the frames followed by a spatial filtering in boxes of size $5\,\lambda/D \times 5\,\lambda/D$. For the TLOCI algorithm, we considered the dual-band data set in each filter separately and performed ADI (Marois et al. 2006a) in order to avoid ambiguities in the photometric calibration (Maire et al. 2014). The data were also binned temporally to reduce the number of frames, hence the computing time. The TLOCI pipeline selected the 80 most correlated frames for which the total self-subtraction, estimated using the measured PSF, was at maximum 70% (Marois et al. 2014). Then it found the best linear combination for subtracting the speckles in annuli of width ~1 full width at half maximum (FWHM). Finally, we derotated the frames to align north up and median-combined them (Fig. 1, right).

The relative photometry of HD 1160 BC was derived using the method of the "negative synthetic companions" (Marois et al. 2010a; Bonnefoy et al. 2011). We subtracted a synthetic companion in the preprocessed data at the measured location of the companions based on the median of the observed PSF (Sect. 2). We then processed the data assuming the TLOCI coefficients computed on the data without the synthetic companions to account for the ADI biases. The subpixel position and the flux of the modeled images were adjusted to optimize the subtraction of the model to the real image within a disk of radius 1.5 FWHM centered on the real image. For the photometry, the $1\sigma$ error bar of the fitting was the excursion that increased the residuals in the 1.5-FWHM area by a factor of $\sqrt{2}$. This factor was empirically determined in Galicher & Marois (2011). The error bars include the variations in the PSF, the variations in the stellar flux during the sequence (estimated from the intensity fluctuations of the stellar residuals), and the fitting accuracy of the model companion images to their measured images. For the relative photometry of PZ Tel B, the same sources of error are included in the error bars, except for the fitting error.

The astrometry of the companions was measured in the coronagraphic images with the satellite spots. These images were corrected for the distortion of the telescope and the instrument (Sect. 3.6). The astrometric calibration is described in Sect. 3.6.

We report the measured relative photometry and astrometry in Tables 2 and 3. For the photometry of PZ Tel B in the $H23$ filter pair, we only considered the July 2014 data set, because the October 2014 observation was a short technical test so the data quality was poorer. For the updated orbital analysis of PZ Tel B (Sect. 6), we only considered the IRDIS $H2$ measurement obtained in July 2014.

The S/N map was estimated using the TLOCI pipeline. Each pixel value was divided by the standard deviation of the flux inside the annulus of same angular separation with a 1 FWHM width. The algorithm throughput was accounted for by injecting synthetic companions in the preprocessed data at regular separations between 0.15″ and 6″ and performing the TLOCI analysis. The process was repeated several times using different position angles in order to average the effects of random speckle residuals in the estimation of the algorithm throughput. The S/N maps were used to derive the detection curves (Sect. 7).

### 3.2. IRDIS LSS

The LRS and MRS data of PZ Tel were reduced in a similar way. The reduction and analysis procedures are very similar to those presented in Hinkley et al. (2015a). A standard set of calibration data (dark, flat field, bad pixel maps) was produced using the preliminary release (v0.14.0−2) of the Data Reduction and Handling software (DRH, Pavlov et al. 2008), the official pipeline of the SPHERE instrument. Then the science frames were dark-subtracted and divided by the flat field. Bad pixels were replaced with the median of neighboring good pixels. The remaining bad pixels were filtered using a sigma-clipping algorithm. Each of the science frames were combined using a median, producing a 2D spectrum from which the companion signal was extracted.

For the subtraction of the stellar halo and speckles at the position of the companion, we compared two approaches that gave similar results. The first method was based on spectral differential imaging (Racine et al. 1999; Sparks & Ford 2002) adapted for LSS data, as presented in Vigan et al. (2008) and demonstrated on-sky in Vigan et al. (2012a). The second technique was much simpler and consisted of subtracting the symmetric part of the halo at the position of the companion with respect to the star. Given that the level of the halo and speckles was a factor ~18 fainter than the peak signal of the companion, this approach gave good results and introduced a negligible bias after the subtraction.

The 1D spectrum of the companion and the off-axis primary were extracted in the following way: for each spectral channel, the signal was summed in an aperture centered on the object position with a width of $\epsilon\,\lambda/D$. When $\epsilon$ was varied from 0.5 to 1.0, there were only very small variations in the output spectrum. The local noise was estimated by summing the residual speckle noise in an aperture at the same separation as the companion, but on the other side of the primary. We checked that

the spectra extracted with the two subtraction schemes and the different aperture sizes lay within these error bars.

The flux spectrum of the companion was converted into a contrast spectrum by dividing by the flux spectrum of the primary extracted in an aperture of the same width. To properly measure the contrast, we took the transmission of the neutral density filter used for acquiring the off-axis PSF data into account. The neutral density filter used for the LRS and MRS observations had an average transmission of 1/3160 and 1/100, respectively (see note 1).

The comparison of the LSS spectra of PZ Tel B to those of late-M objects (Sect. 5.2) and those obtained with the SINFONI instrument (Sect. 3.3.2) revealed a residual error in wavelength dispersion relation of the SPHERE spectra. For the MRS spectrum, we fitted a new dispersion relation matching ten telluric features with those found into a synthetic spectrum of the Earth atmosphere transmission curve (Noll et al. 2012; Jones et al. 2013). For the LRS spectrum, we applied a linear correction factor to the wavelengths derived by the DRH pipeline. The factors were found by comparing the PZ Tel B LRS spectrum to the SINFONI spectrum and to the spectrum of the M8 standard VB10 (van Biesbroeck 1961; Burgasser et al. 2004).

### 3.3. IFS spectroscopy

#### 3.3.1. SPHERE IFS

The raw data were preprocessed using the SPHERE DRH software (Pavlov et al. 2008) up to the extraction of the calibrated data cubes. The design of the SPHERE IFS differs in two main points from the IFS of the high-contrast exoplanet imagers P1640 and GPI. First, the cross talk between adjacent pixels is minimized (Antichi et al. 2009). Then, the spectra are aligned with the detector columns (see Fig. 2 in Mesa et al. 2015). These differences allow for a simpler reduction procedure for the SPHERE IFS data, which does not rely on determining the instrument PSF (Zimmerman et al. 2011; Perrin et al. 2014).

The raw data were first corrected for the dark and the detector flat. Then the positions of the spectra were defined from an image in which the whole integral field unit (IFU) was uniformly illuminated with a white calibration lamp. Each pixel of the detector was assigned a first-guess wavelength. In a second step, the wavelength was further refined based on the illumination of the IFU with three (resp. four) monochromatic lasers with known wavelength for the $YJ$ (resp. $YJH$) data. Finally, the data cubes (science, PSF, and satellite spots) were extracted and corrected for the variations in the response of the IFU lenslets. Each data cube had 39 monochromatic images. Right before the extraction of the spectral data cubes, an additional step exploiting custom IDL routines (Mesa et al. 2015) was performed for improving the correction of the bad pixels and spectral cross-talk.

We used the coronagraphic images with the satellite spots (Sect. 2) of the data sets listed in Table 1 to obtain the astrometry of PZ Tel B and HD 1160 B (Table 3).

For extracting the spectrum of the companions, we considered each spectral channel separately and performed derotation and median-stacking of the frames (Fig. 2). For the purpose of searching for additional companions in the system, we also considered each spectral channel separately but subtracted the stellar residuals with a principal component analysis approach (PCA, Soummer et al. 2012; Amara & Quanz 2012), as illustrated in Maire et al. (2014).

The 1D detection limits (Sect. 7) were derived as the standard deviation of the residual flux in annuli of 1 $\lambda/D$ width at each angular separation. We estimated the PCA subtraction of off-axis point sources using synthetic companions injected into the preprocessed data at several separations and position angles. We optimized the number of PCA modes to maximize the detection performance.

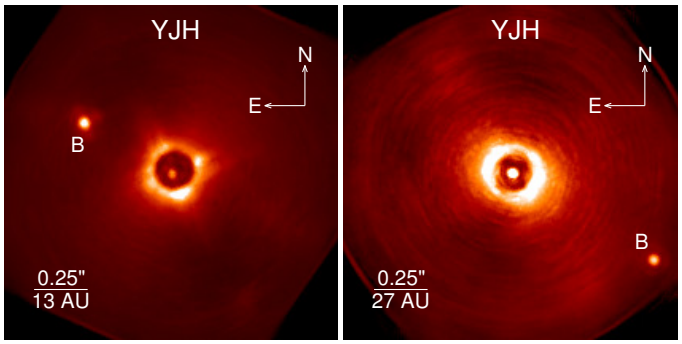


**Fig. 2.** IFS median-collapsed images of PZ Tel B (*left*) and HD 1160 B (*right*) after derotation and stack of the temporal frames. The square root intensity scales have different ranges.

#### 3.3.2. SINFONI spectra of PZ Tel B

We reduced the data corresponding to the SINFONI observations of PZ Tel B (Sect. 2.4) with the ESO data reduction pipeline (Modigliani et al. 2007) version 2.5.2. The pipeline built the bad pixel mask and flat field associated to each observation date and setup. It corrected each raw frame for the instrument distortion, derived a map of wavelength associated to each detector pixel, and found the position of the spectra (slitlets) on the detector. After these steps, we obtained the final data cube from the raw 2D science frames. For the August 2011 data, the sky emission was evaluated and removed using exposures of an empty field obtained during the observation sequence. No sky exposure was obtained for the remaining observations. Therefore, we instead subtracted a dark frame from the raw science images in order to remove the bias and the detector ramp effect, and applied the algorithms of Davies (2007) implemented into the pipeline to remove the sky contribution (thermal background and emission lines).

PZ Tel A was located inside the field of view of the instrument for the September 2011 observations. This was not the case for the August 2011 observations (Schmidt et al. 2014), for which the PSF core of PZ Tel A was located a few pixels outside the field of view. We removed the stellar halo using a radial profile for both cases. For the August 2011 data, we chose the approximate star position that minimized the halo residuals. The companion was always masked (circular mask of radius 7 pixels) while computing the radial profile.

The flux of PZ Tel B was measured in the halo-removed data cubes using aperture photometry (circular aperture of radius 5 or 6 pixels). The aperture radius was determined by eye with respect to the encircled energy of a given observation and the level of residuals from the halo subtraction close to the companion. All extracted spectra were corrected for telluric absorptions using those of B-type standard stars observed after PZ Tel (hereafter Method 1). For the case of the data acquired on Sept. 11, 2014, we also used the spectrum of PZ Tel A extracted with circular apertures of similar size as an alternative correction (hereafter Method 2). This enabled the estimation of a companion-to-star contrast ratio at each wavelength that can be compared directly to the SPHERE spectra and that was less sensitive to

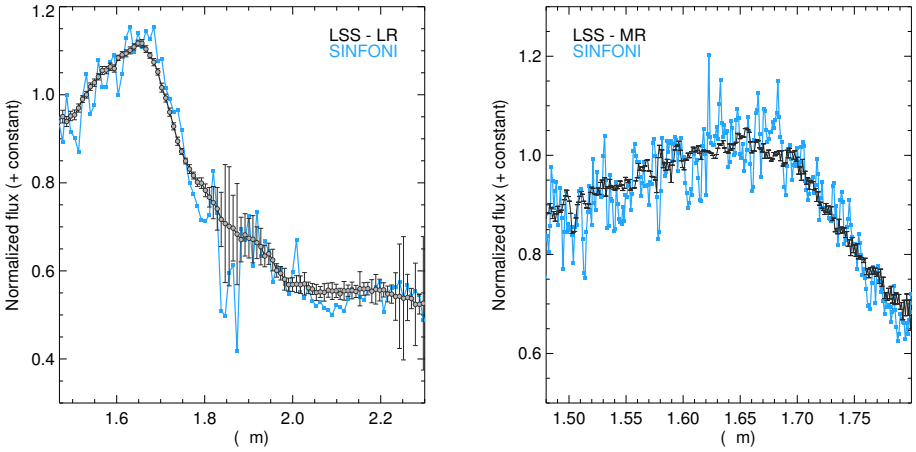


**Fig. 3.** Comparison of the SINFONI $H+K$ band spectrum and the SPHERE long-slit spectra of PZ Tel B at comparable resolutions.

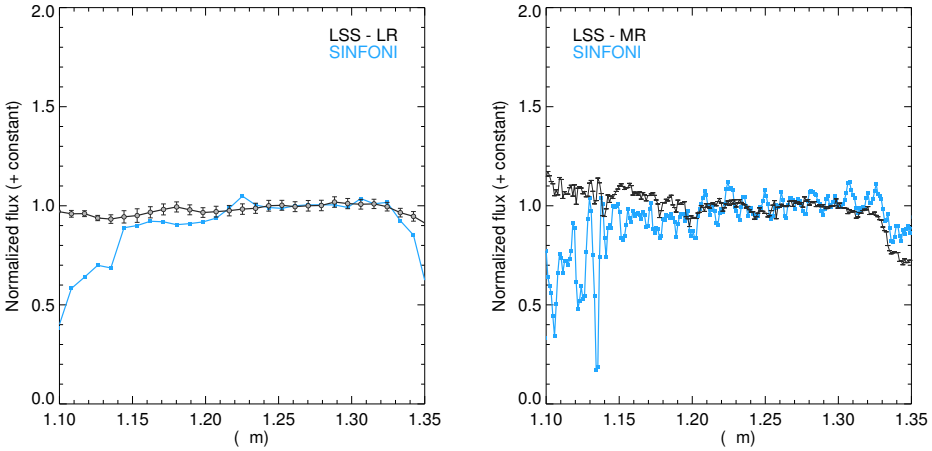


**Fig. 4.** Comparison of the SINFONI and the SPHERE long-slit spectra of PZ Tel B in the $J$ band.

differential flux losses due to the limited size of the apertures. We converted the contrast obtained following Method 2 to a flux-calibrated spectrum following the method described in Sect. 5.1.

Both methods give results that agree within error bars estimated from the standard deviation of the flux at each wavelength obtained from the different epochs. The $HK$-band spectrum obtained with Method 1 benefits from the increased exposure time from all combined data sets. It looks identical to the spectrum obtained by Schmidt et al. (2014) except for the 1.45−1.6 $\mu$m range, where it has less pronounced $H_2O$ absorptions. It nevertheless reproduces all the features of the low-resolution LSS spectra of the source obtained with SPHERE well (Fig. 3).

The $J$-band SINFONI spectrum and low-resolution LSS spectrum of PZ Tel B have an identical slope from 1.2 to 1.3 $\mu$m (Fig. 4). The LSS spectrum is, however, not affected by strong telluric residuals shortward of 1.2 $\mu$m, which probably arise from an improper subtraction of the stellar halo in the SINFONI data at these wavelengths. The medium-resolution LSS spectrum has a bluer slope than the SINFONI spectrum. The origin of this slope is unclear. The preprocessed data were checked for saturation and contamination by the star signal. We are still analyzing the data, as well as other LSS data sets from the commissioning runs, to determine the science performance and limitations of this observing mode. The results will be presented in a forthcoming paper. The SPHERE spectra supersede the SINFONI spectrum inside this wavelength range because of their higher S/N at a comparable spectral resolution.

### 3.4. ZIMPOL imaging

The raw data were preprocessed using the SPHERE DRH software (Pavlov et al. 2008). This included bias subtraction and flat-fielding with coronagraphic flats taken after the science sequences, as well as ZIMPOL specific tasks, such as the cropping of the image and the interpolation of pixels in the image $y$ direction in order to produce a square image. Using the timestamps in the image header, for each individual exposure the parallactic angle was computed and the images combined using a simple ADI approach (Marois et al. 2006a). A reference image of the stellar signature was generated by median combination of all preprocessed images. Owing to the field rotation during the pupil-stabilized observations, the large majority of the flux of the companion was rejected in this process. This reference image of the stellar signature was then subtracted from all individual frames, which were subsequently derotated to align north up and combined. The true north was estimated using the IRDIS astrometry of the companion measured during the same run. Since the coordinate system in ZIMPOL camera 1 is flipped in the $y$ direction with respect to the sky, all $R'$-band images were first flipped in the $y$ direction before derotation and image combination. The resulting images are shown in Fig. 5.

We used relative aperture photometry to measure the flux of PZ Tel B in both bands. For all measurements, the Aperture Photometry Tool (Laher et al. 2012) was utilized. The aperture size was set to a radius of five pixels for all measurements. This was chosen to exclude the bright diffraction-related features in

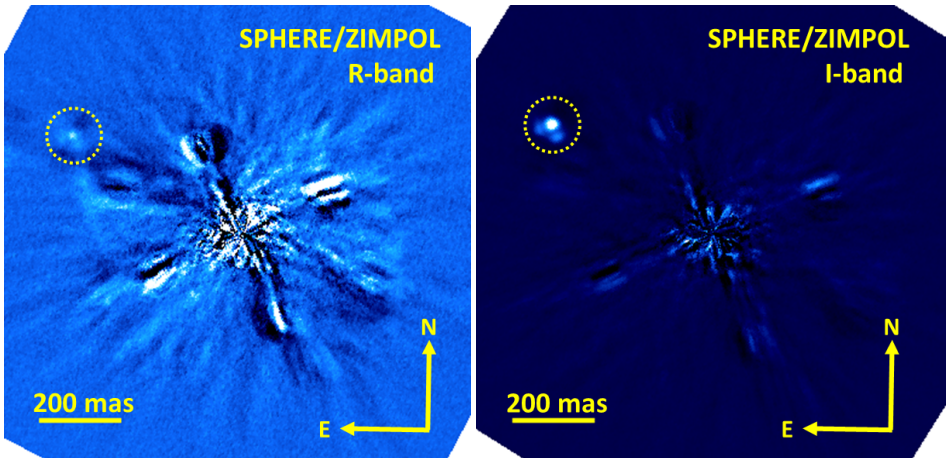


**Fig. 5.** ADI-reduced $R'$-band and $I'$-band coronagraphic ZIMPOL images of PZ Tel B obtained simultaneously in the imaging mode (see text). The companion is marked in both images with a dashed circle. The artifact seen around the companion signal in both images is due to an intermittent instrumental effect currently under study, possibly related to the telescope.

the companion PSF. The companion flux was measured in the ADI-reduced images, while the star flux was measured in the reference images and then rescaled to the longer observation time of the science images. Care was taken to choose regions for background subtraction that were not contaminated by the stellar halo to avoid oversubtraction. Since ADI imaging suffers from self-subtraction of the companion flux, we corrected for this effect as well. For this purpose, we used the unsaturated images of PZ Tel A to generate fake companion PSF, which we injected in the preprocessed data. We then measured the amount of self-subtraction of these fake planets. Care was taken to inject the fake companions at the same angular separation as the real companion PZ Tel B and various position angles, to ensure similar self-subtraction effects during ADI processing. The resulting photometric measurements are summarized in Table 2. The uncertainties include the statistical uncertainties from the aperture photometry, the uncertainties from the calibration of the ADI self-subtraction, and the temporal variations of the stellar flux during the sequence (measured using one of the simultaneous satellite spots). The self-subtraction uncertainties were estimated according to the range of correction factors calculated from several fake companions. The photometric error due to the PSF variations could not be estimated since only one PSF was recorded. The astrometry of the companion was not considered for this paper, because of the availability of IRDIS and IFS data close in time. The ZIMPOL astrometry will be discussed in a forthcoming paper.

### 3.5. NaCo $L'$-band images of HD 1160

The Keck/NIRC2 $L'$-band images reported in Nielsen et al. (2012) appear to have poorer quality than the NaCo (Nasmyth Adaptive Optics System and Near-Infrared Imager and Spectrograph, Rousset et al. 2003; Lenzen et al. 2003) $L'$-band images obtained at multiple epochs and available in the ESO public archive (ESO program 60.A-9026). We made use of these NaCo images to check the consistency of the Keck/NIRC2 $L'$-band photometry. We reduced five epochs of observations (Dec. 23, 2005; Sept. 17, 2010; Jul. 11, 2011; Sept. 2, 2011; Nov. 8, 2011) with the ESO `Eclipse` software (Devillard 1997). HD 1160 B was resolved at each epoch, but the strehl and residual background close to the star appeared to have better quality in the images obtained in November 2011. We chose to perform aperture photometry (circular apertures of radius 160 mas) on the star and its companion on these images and found $\Delta L'_{\rm B/A} = 6.54 \pm 0.10$ mag and $\Delta L'_{\rm C/A} = 4.69 \pm 0.05$ mag for HD 1160 B and C, respectively. The values were consistent with those derived from the four other epochs within the error bars. The NaCo photometry also agrees within the error bars ($3\sigma$) with the Keck/NIRC2 photometry reported in Nielsen et al. (2012). Nevertheless, we preferred to use the NaCo photometry below, since it enabled a direct comparison to the photometry of PZ Tel B. The NaCo $L'$ photometry brings the $K_{\rm s} - L'$ band color of HD 1160 B ($K_{\rm s} - L' = 0.53 \pm 0.12$ mag) into better agreement with those of mid- to late-M field dwarfs. Using the $L$-band magnitude of HD 1160 A reported in van der Bliek et al. (1996), we found $L'_{\rm B} = 13.60 \pm 0.10$ mag and $L'_{\rm C} = 11.76 \pm 0.05$ mag.

We note that, independently of our new photometry, the $L' - M_{\rm s}$ color of HD 1160 B (Nielsen et al. 2012) appears to be much redder with respect to M or early-L dwarf companions (Fig. 5, Bonnefoy et al. 2014b). Therefore, we decided not to use the Keck/NIRC2 photometry of the system below.

### 3.6. IRDIS and IFS astrometric calibration

The IRDIS astrometric measurements reported in Table 3 were derived using the plate scale and the true north orientation measured for the 47 Tuc data (Table 4). We recall that no relevant observations of astrometric calibrators were obtained for IFS (Sect. 2). For the IFS data we estimated a plate scale of $7.46 \pm 0.01$ mas/pix and a relative orientation to IRDIS data of $-100.46 \pm 0.13°$ from simultaneous data of distortion grids of both instruments. Using this calibration and correcting for the instrument distortion (see below), we estimated the astrometry of the companions in IFS data listed in Table 3.

The 47 Tuc IRDIS data were reduced and analyzed using the SPHERE DRH software (Pavlov et al. 2008) and custom IDL routines. The star positions were measured using the centroid IDL routine `cntrd`[2] derived from the DAOphot software (Stetson 1987). The measured positions were then compared to HST positions corrected for the differential proper motions of the individual stars between the HST observations (March 13, 2006) and the SPHERE observations (Bellini & Anderson, priv. comm.; see Bellini et al. 2014, for the description of the methods used for deriving the catalog positions and the individual stellar proper motions). The typical accuracy of the catalog positions is ~0.3 mas and takes the time baseline between the HST and SPHERE observations into account. Typically, more than 50 stars were cross-identified and used for the analysis. The distortion measured on-sky is dominated by an anamorphism ($0.60 \pm 0.02\%$) between the horizontal and the vertical directions

[2] `http://idlastro.gsfc.nasa.gov/ftp/pro/idlphot/`

**Table 4.** Mean plate scale and true north orientation for the SPHERE commissioning runs measured on the 47 Tuc field-stabilized observations in the IRDIS images in the *H*23 filter pair obtained with the APLC coronagraph (Sect. 2).

| | *H*2 | | *H*3 | |
|---|---|---|---|---|
| Com. date | Plate scale (mas/pix) | True north (°) | Plate scale (mas/pix) | True north (°) |
| July 2014 | 12.252 ± 0.006 | −1.636 ± 0.013 | 12.247 ± 0.006 | −1.653 ± 0.005 |
| August 2014 | 12.263 ± 0.006 | −1.636 ± 0.013 | 12.258 ± 0.006 | −1.653 ± 0.005 |
| October 2014 | 12.259 ± 0.006 | −1.788 ± 0.008 | 12.254 ± 0.005 | −1.795 ± 0.008 |

**Notes.** To align the IRDIS science images so that north is oriented up and east left, an offset accounting for the zeropoint of the derotator in pupil-stabilized mode of 135.87 ± 0.03° has to be added to the parallactic angles indicated in the fits header. This offset is measured on data of 47 Tuc acquired in July 2014 in both stabilization modes and assumed to be constant between the runs. For the astrometric calibration of the IFS science images, an additional offset accounting for the relative orientation between the IFS and IRDIS fields of −100.46 ± 0.13° also has to be added. This value is measured on simultaneous data of distortion grids of both instruments.

**Table 5.** Comparison stars used for the REM photometry.

| | Name | RA (J2000.0) (hh mm ss) | Dec (J2000.0) (° ′ ″) | *V* (mag) |
|---|---|---|---|---|
| C1 | TYC 8381-2548-1 | 18 52 55.39 | −50 09 13.26 | 10.487 ± 0.016 |
| C2 | CD-50 12193 | 18 53 28.02 | −50 13 08.26 | 10.173 ± 0.015 |
| C3 | 2MASS J18531926-5014042 | 18 53 19.26 | −50 14 04.20 | 12.233 ± 0.060 |

of the detector. The on-sky distortion is similar to the distortion measured in laboratory, suggesting that the distortion from the telescope is negligible with respect to the distortion of SPHERE. The anamorphism is produced by cylindrical mirrors in the common path and infrastructure of the instrument, hence common to IRDIS and IFS, except that the anamorphism is rotated for the IFS data. The plate scale and the true north orientation given in Table 4 were corrected for the anamorphism.

## 4. Updated photometry of PZ Tel A

Young, late-type stars are known to show photometric variability on several timescales, hourly due to flares, daily due to rotational modulations of active regions on the stellar surface, and on longer timescales due to, for instance, reconfiguration of active regions and activity cycles. Long-term variations of these stars were studied less intensively than short-term variations due to the long time baseline needed for the analysis.

The characterization of substellar objects like those presented in this paper are typically obtained differentially with respect to the host stars. Ideally, the magnitude of the host star should be derived simultaneously to the high-angular resolution observations, but this is difficult to achieve in practice. Photometric monitoring in the same observing season as the high-contrast observations insures that the latter are properly calibrated. From the analysis of literature data (Sect. 4.4), PZ Tel A is shown to have photometric variations of up to 0.2 mag over several decades. We present below new photometric observations of the star taken in the same season as the SPHERE data and the study of its photometric variability on various timescales.

### 4.1. REM observations

We observed PZ Tel A with the 60-cm Rapid Eye Mount (REM, Chincarini et al. 2003) telescope (La Silla, ESO, Chile) with both the NIR REMIR and the optical ROS2 cameras. The REMIR camera hosts a 512 pix × 512 pix CCD and has a field of view of 10′ × 10′ and a plate scale of 1.2″/pix. The ROS2 camera hosts a 2048 pix × 2048 pix CCD and has a field of view of 8′ × 8′ and a plate scale of 0.58″/pix. We could observe the star from October 29, 2014 until December 5, 2014 for a total of 30 nights. After discarding frames collected in very poor seeing conditions and frames missing one or more comparison stars (due to inaccurate telescope pointing), we were left with a total of 173, 131, and 133 frames in the *J*, *H*, and *K* filters, respectively, and 205, 166, and 219 frames in the *g*, *r*, and *i* filters. The exposure time was fixed to 1 s in the ROS2 camera, whereas five consecutive dither frames of 1 s each were collected with the REMIR camera on each telescope pointing. All frames were first bias-subtracted and then flat-fielded. Aperture photometry was used to extract the magnitudes of PZ Tel A and other stars in the field to be used as comparison stars. All reduction steps were performed using the tasks within IRAF[3]. After removing a few outliers from the magnitude time series, using a 3$\sigma$ filtering, we averaged consecutive data collected within one hour, and finally we were left with 24, 18, and 19 averaged magnitudes in the *J*, *H*, and *K* filters, respectively, and 38, 26, and 34 averaged magnitudes in the *g*, *r*, and *i* filters, respectively.

The mean standard deviations associated to the average magnitudes were $\sigma_J = 0.017$, $\sigma_H = 0.018$, $\sigma_K = 0.013$ mag, and $\sigma_g = 0.035$, $\sigma_r = 0.021$, $\sigma_i = 0.018$ mag. Analyzing the All Sky Automated Survey (ASAS, Pojmanski 1997) photometric time-series of the brighter stars in the field of PZ Tel A, we identified three stars (Table 5) whose light curves were very stable, and they were therefore suitable as comparison stars. Their differential magnitudes also during our observing run were found to be constant within our photometric precision in both optical and the NIR photometric bands (Table 6).

We compared the average differential values of the comparison stars (C1−C2, C1−C3, and C2−C3) with respect to the differential values derived from the Two Micron All Sky Survey (2MASS, Cutri et al. 2003) listed in Table 7. Table 6 lists the differential values. We note that they are all consistent with each other within the uncertainties, verifying that these stars do not vary also in the NIR. Only the comparison star C3 exhibits

[3] IRAF is distributed by the National Optical Astronomy Observatory, which is operated by the Association of the Universities for Research in Astronomy, Inc. (AURA) under cooperative agreement with the National Science Foundation.

**Table 6.** Average differential magnitudes from 2MASS catalog and REM observations.

| | 2MASS (mag) | REM (mag) | Filter |
|---|---|---|---|
| C1−C2 | 1.00 ± 0.04 | 1.01 ± 0.03 | *J* |
| C1−C3 | −0.24 ± 0.04 | −0.26 ± 0.04 | *J* |
| C2−C3 | −1.24 ± 0.03 | −1.26 ± 0.02 | *J* |
| C1−C2 | 1.12 ± 0.06 | 1.17 ± 0.03 | *H* |
| C1−C3 | −0.01 ± 0.05 | −0.02 ± 0.04 | *H* |
| C2−C3 | −1.13 ± 0.04 | −1.17 ± 0.04 | *H* |
| C1−C2 | 1.28 ± 0.03 | 1.25 ± 0.02 | *K* |
| C1−C3 | 0.13 ± 0.04 | 0.11 ± 0.03 | *K* |
| C2−C3 | −1.14 ± 0.03 | −1.12 ± 0.02 | *K* |

**Table 7.** 2MASS magnitudes of comparison stars adopted to calibrate the REM magnitudes.

| | *J* (mag) | *H* (mag) | *K* (mag) |
|---|---|---|---|
| C1 | 8.493 ± 0.035 | 7.904 ± 0.044 | 7.801 ± 0.029 |
| C2 | 7.495 ± 0.023 | 6.781 ± 0.036 | 6.525 ± 0.020 |
| C3 | 8.734 ± 0.023 | 7.915 ± 0.020 | 7.667 ± 0.023 |

slightly larger magnitude variations with respect to the 2MASS values. More precisely, it remained constant during the observation run, but probably has a long-term (on the order of years) small amplitude variation.

Once we checked that the comparison stars were not variable, we could use the C1 and C2 2MASS magnitudes (Table 7) to transform the PZ Tel A differential magnitudes into absolute values. We finally obtained the average magnitudes: $J = 6.84 \pm 0.04$ mag, $H = 6.430 \pm 0.045$ mag, and $K = 6.27 \pm 0.03$ mag in the NIR, $g = 8.51 \pm 0.04$ mag, $r = 8.11 \pm 0.04$ mag, and $i = 7.70 \pm 0.04$ mag in the optical.

### 4.2. York Creek Observatory observations

PZ Tel A was observed from November 18, 2014 to December 2, 2014, for a total of six nights at the York Creek Observatory (41° 06′ 06″S; 146° 50′ 33″E, Georgetown, Tasmania) using a f/10 25-cm Takahashi Mewlon reflector, equipped with a QSI 683ws-8 camera, and *B*, *V*, and *R* standard Johnson-Cousins filters. The telescope has a field of view of 24.5′ × 18.5′. The plate scale is 0.44″/pix. A total of 48 frames in each filter were collected using an integration time of 30 s. Data reduction was performed as described in the previous section for the REM data. The photometric accuracies we could achieve are $\sigma_B = 0.009$, $\sigma_V = 0.007$, and $\sigma_R = 0.006$ mag. We derived new photometry for PZ Tel A using the differential *B*, *V*, and *R* light curves of the star, as well as literature *B* and *V* magnitudes of the comparison stars C1 and C2 (see Sect. 4.1). The average magnitudes are $B = 9.05 \pm 0.05$ mag and $V = 8.30 \pm 0.05$ mag.

### 4.3. Rotation period search

We used the Lomb-Scargle (Scargle 1982) and CLEAN (Roberts et al. 1987) periodogram analyses on our own observations to search for the rotation period of PZ Tel A. As expected, we found that the star exhibits variability in all bands. A correlation study showed that the magnitude variations among all $J+H+K$ bands are correlated ($r_{JH} = 0.70$, $r_{JK} = 0.42$, $r_{HK} = 0.84$ mag) with significance level >99% (with the *H* and *K* magnitudes exhibiting a higher degree of correlation) and also among all $g + r + i$ bands ($r_{gr} = 0.87$, $r_{gi} = 0.53$, $r_{ri} = 0.46$ mag) with significance level of >95% (with the *r* and *i* magnitudes exhibiting a smaller degree of correlation). To improve the S/N of our time series, we built a new light curve by averaging the *H* and *K* light curves (which is justified by the high correlation between the light curves) and by averaging the *g*, *r*, and *i* light curves.

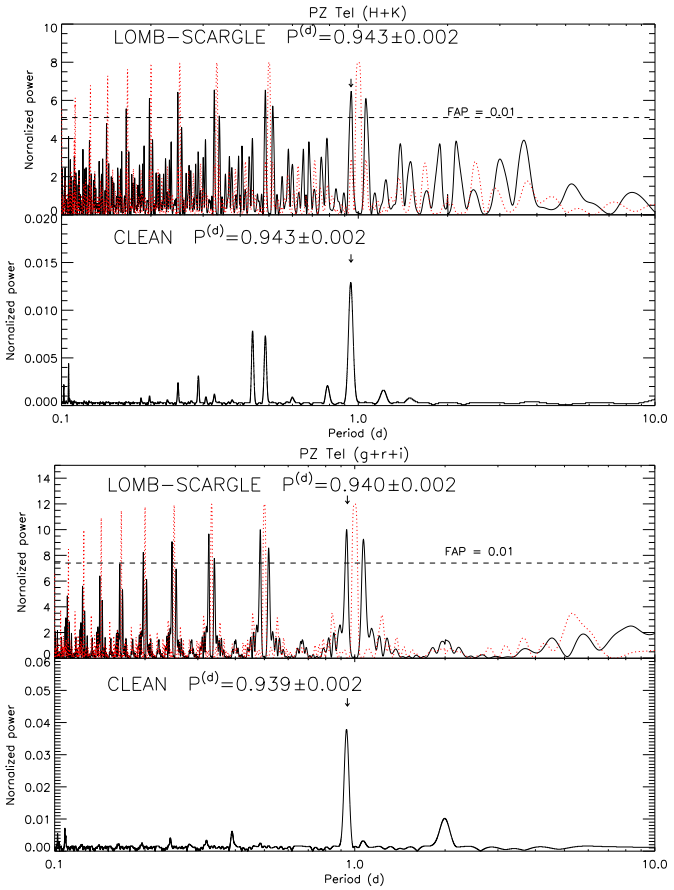


**Fig. 6.** LS and CLEAN periodograms of the *H*+*K* timeseries (*top panels*) and of the *g*+*r*+*i* timeseries (*bottom panels*) (see text).

Both LS and CLEAN periodograms showed that the major power peak in the averaged NIR light curve is at $P = 0.943 \pm 0.002$ d and with false alarm probability FAP < 1%. The FAP, which is the probability that a power peak of that height simply arises from Gaussian noise in the data, was estimated using a Monte-Carlo method, i.e., by generating 1000 artificial light curves obtained from the real one, keeping the date but scrambling the magnitude values. The results are summarized in Fig. 6, where in the top panels we plot the LS periodograms and the CLEAN periodograms in the lower panels. In the LS periodogram we also note a number of secondary power peaks at a high significance level. These peaks are beats of the rotation period according to the relation $B = (1/P) \pm n$, where *B* is the beat period and *n* an integer. They arise from a one-day sampling interval imposed by the rotation of the Earth and the fixed longitude of the observation site. It can be noted that in the CLEAN periodograms, the power peak arising from the light rotational modulation dominates, whereas all secondary peaks are effectively removed. The horizontal dashed line indicates the power level associated to a FAP = 1%, whereas the red dotted line shows the spectral window arising from the data time sampling.

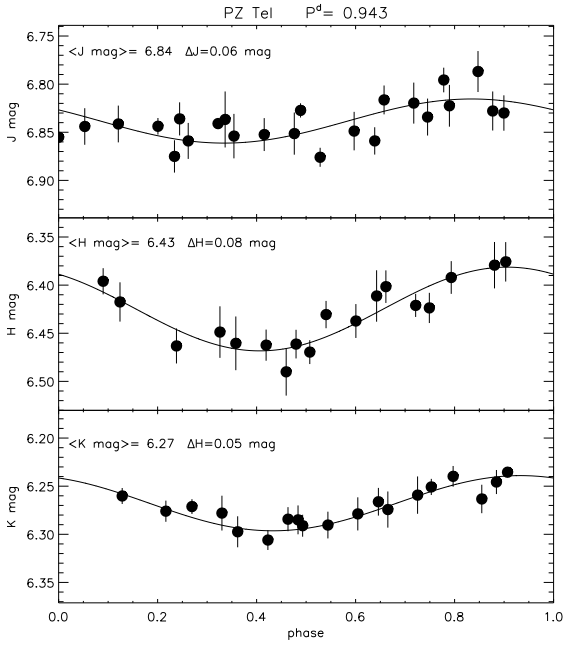


**Fig. 7.** $J$, $H$, and $K$ light curves of PZ Tel A collected with the REM telescope and phased with the $P = 0.943$ d rotation period. Sinusoidal fits are overplotted (solid lines). Average magnitude and peak-to-peak amplitudes are given in the labels.

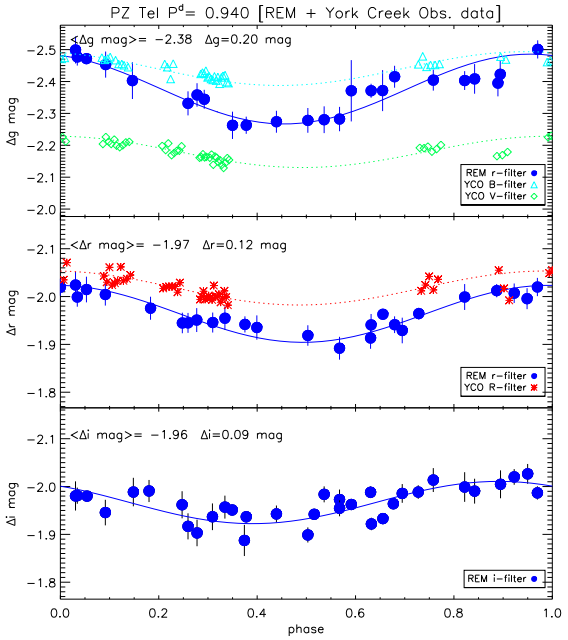


**Fig. 8.** $g$, $r$, and $i$ light curves of PZ Tel A collected with the REM telescope (blue bullets) and phased with the $P = 0.940$ d rotation period. Sinusoidal fits are overplotted (solid lines). Average magnitudes and peak-to-peak amplitudes are given in the labels. Triangles, diamonds, and asterisks represent the $B$, $V$, and $R$ data, respectively, collected at the York Creek Observatory.

In Fig. 7, we plot the NIR light curves of PZ Tel A that are phased with the 0.943-d rotation period. Solid lines are sinusoidal fits with the rotation period. The amplitude of the light curves (measured from the amplitude of the sinusoid) are $\Delta J = 0.06$, $\Delta H = 0.08$, and $\Delta K = 0.05$ mag.

The same periodogram analysis in the composed optical light curve showed that the major power peak is at $P = 0.940 \pm 0.002$ d and with FAP < 1%. In Fig. 8, we plot the optical $g$, $r$, and $i$ light curves of PZ Tel A that are phased with the 0.940-d rotation period. Solid lines are sinusoidal fits with the rotation period. The amplitudes of the light curves are $\Delta g = 0.20$, $\Delta r = 0.12$, and $\Delta i = 0.09$ mag.

$B$, $V$, and $R$ data also indicate that PZ Tel A is variable (Fig. 8). However, owing to the short data set, we did not search for the rotation period. They appear to be well in phase with the $g$, $r$, and $i$ light curves, although the light curve minimum was uncovered by the observations. From the sinusoidal fits, we infer the light curve amplitudes: $\Delta B = 0.11$, $\Delta V = 0.10$, and $\Delta R = 0.07$ mag.

### 4.4. Literature information

The rotation period of PZ Tel was first discovered by Coates et al. (1980, 1982) who found $P = 0.942$ d. More precise determinations were subsequently obtained by Lloyd Evans & Koen (1987; $P = 0.9447$ d), by Innis et al. (1990; $P = 0.94486$ d), and Cutispoto (1998; $P = 0.9447$ d). Most recently, a period $P = 0.9457$ d was derived by Kiraga (2012) from the analysis of about ten years of ASAS photometry. The fast rotation is consistent with the very high values of the projected rotational velocity reported in the literature by various authors. Randich et al. (1993) measure $v \sin i = 70$ km s$^{-1}$, Soderblom et al. (1998) $v \sin i = 58$ km s$^{-1}$, Barnes et al. (2000) $v \sin i = 68$ km s$^{-1}$, Cutispoto et al. (2002) $v \sin i = 70$ km s$^{-1}$, de la Reza & Pinzón (2004) $v \sin i = 67$ km s$^{-1}$, Torres et al. (2006) $v \sin i = 69$ km s$^{-1}$, and Scholz et al. (2007) $v \sin i = 77.50$ km s$^{-1}$. Assuming an unspotted magnitude $V = 8.25$ mag, derived from our own photometry, a distance $d = 47 \pm 7$ pc from HIPPARCOS, a bolometric correction $BC_V = -0.26$ mag, and $T_{\rm eff} = 5210$ K from Pecaut & Mamajek (2013), we derive a luminosity of $L = 1.16 \pm 0.10\, L_\odot$ and a radius $R = 1.32 \pm 0.14\, R_\odot$. Combining stellar radius and rotation period, we infer an inclination for the stellar equator (with respect to the direction perpendicular to the line of sight) from the standard formula $\sin i = (P \times v \sin i)/(R \times k)$, where $k$ is a constant $k = 50.578$, $R$ in solar units, $P$ in days, and $v \sin i$ in km s$^{-1}$. We find $75° < i < 90°$; i.e., we see PZ Tel A almost from its equator.

This configuration generally allows a large rotational modulation of the spot visibility, producing light variations with large amplitudes. However, when we compare the stellar average light curve amplitude ($\Delta V = 0.10$ mag), we see that it lies close to the lower boundary of the light curve amplitude distributions of the $\beta$ Pic members (see Messina et al. 2010). We have only one season (1982.47) when the star exhibited a light curve amplitude $\Delta V = 0.22$ mag. A reasonable scenario that we can draw from the available photometry is that PZ Tel A has a dominant fraction of spots or spot groups, either uniformly distributed in longitude or located at very high latitudes, which is decreasing in time, making the star brighter. PZ Tel A also possesses a smaller fraction of spots unevenly distributed in longitude that accounts for the relatively small light curve amplitude generally observed.

In Fig. 9, we plot the complete series of $V$-band magnitudes, spanning a time interval of almost 38 yr. Data were retrieved from a number of sources: Lloyd Evans & Koen (1987), Coates et al. (1980), and Innis et al. (1983) who collected data at SAAO; Cutispoto & Leto (1997) and Cutispoto (1998) who collected data at ESO; the HIPPARCOS Epoch photometry data (ESA 1997); the ASAS public archive (Pojmanski 1997); and Innis et al. (2007). We note that the star exhibits long-term variability,

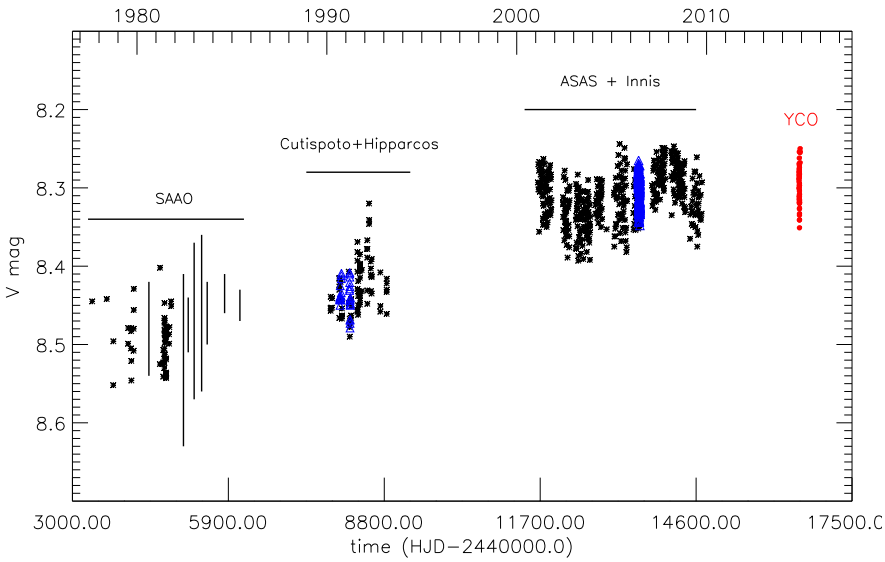


**Fig. 9.** Historical 38-yr long time series of $V$-band magnitudes of PZ Tel A from 1977 to present. Vertical bars denote epochs for which only brightest and faintest magnitudes are available in the literature.

with a brightening of the average magnitude of ∼0.25 mag during the last 38 yr, reaching the brightest value $V = 8.25$ mag in the most recent years. The light curve amplitude has remained about constant, whereas the component of spots uniformly distributed in longitude has gradually decreased, as if PZ Tel A was approaching some sort of starspot activity minimum.

## 5. Physical properties of PZ Tel B and HD 1160 BC

### 5.1. Conversion to fluxes

The contrast factors extracted for the companions from the IFS and IRDIS data in Sect. 3 were converted to fluxes in order to allow for a characterization of their SED. We first fit a synthetic spectrum from the GAIA-COND library (Brott & Hauschildt 2005) onto the photometry of PZ Tel A and HD 1160 A:

- For the fitting of the photometry of PZ Tel A, only the $J$, $H$, and $K$ band photometry derived in Sect. 4.1 was used. It appears close to the 2MASS values (Cutri et al. 2003). This indicates that it is not deeply affected by the photometric variability of the star, contrary to the optical photometry reported in the same section. The photometry was converted to fluxes using the REM instrument passbands and a flux-calibrated model spectrum of Vega (Castelli & Kurucz 1994). We investigated the effect of the atmospheric extinction using the sky simulator[4] SKYCALC (Noll et al. 2012; Jones et al. 2013) and found it to be negligible. We considered models with $T_{\rm eff}$ in the range 5000−5600 K, $\log(g)$ between 3.5 and 5.5 dex, and [Fe/H] = 0 dex, for example, with atmospheric parameters bracketing the different values reported in Allende Prieto & Lambert (1999), Ammons et al. (2006), Mentuch et al. (2008), Soubiran et al. (2010), Bailer-Jones (2011). A best fit was reached for $T_{\rm eff} = 5000$ K and $\log(g) = 4.0$ dex.
- The HD 1160 A 0.4−22 $\mu$m SED was built from Kharchenko (2001), Cutri et al. (2003, 2013). A model with $T_{\rm eff} = 9200$ K and $\log(g) = 4.0$ dex provided the best fit to the apparent fluxes.

These flux-calibrated stellar spectra were used to retrieve the companion spectra. We also used them to determine the fluxes of the components of HD 1160 in the IRDIS passbands (Table 8) from the definition of the passbands in Vigan et al. (2016).

The remaining photometric data points of PZ Tel B were converted using a dedicated procedure. We used the model spectrum of the host star, a model spectrum of Vega, and the atmospheric transmission (SKYCALC) to estimate a photometric shift between the measured ZIMPOL and ROS2 and the IRDIS and REMIR photometry. We applied the same procedure to re-estimate the magnitude of the star and the companion in the NaCo $J$, $H$, $K$ band filters and the NICI $CH_4$ 1% and $H_2$ 1−0 filters (Biller et al. 2010). The companion magnitudes were then

**Table 8.** Available photometry for HD 1160 B and C.

| Filter | $\lambda$ ($\mu$m) | $\Delta\lambda^a$ ($\mu$m) | $F_\lambda$ ($10^{-15}$ W m$^{-2}$ $\mu$m$^{-1}$) B | C |
|---|---|---|---|---|
| $J$ | 1.250 | 0.180 | 1.361 ± 0.131 | 13.861 ± 0.520 |
| $H$ | 1.650 | 0.290 | 1.582 ± 0.121 | 11.047 ± 0.309 |
| $K1$ | 2.110 | 0.105 | 1.152 ± 0.054 | 5.411 ± 0.307 |
| $K_s$ | 2.200 | 0.330 | 0.938 ± 0.044 | 5.605 ± 0.318 |
| $K2$ | 2.251 | 0.112 | 1.127 ± 0.042 | 4.964 ± 0.186 |
| $L'$ | 3.800 | 0.620 | 0.196 ± 0.019 | 1.078 ± 0.051 |

**Notes.** [(a)] Full width at half maximum.

**Table 9.** Available photometry for PZ Tel B.

| Filter | $\lambda$ ($\mu$m) | $\Delta\lambda^a$ ($\mu$m) | Magnitude (mag) | $F_\lambda$ ($10^{-14}$ W m$^{-2}$ $\mu$m$^{-1}$) |
|---|---|---|---|---|
| $R'$ | 0.626 | 0.149 | $17.84^{+0.22}_{-0.31}$ | $0.18^{+0.06}_{-0.03}$ |
| $I'$ | 0.790 | 0.153 | 15.16 ± 0.12 | 1.04 ± 0.12 |
| $J$ | 1.265 | 0.250 | 12.47 ± 0.20 | 3.07 ± 0.62 |
| $CH_4$ 1% | 1.587 | 0.015 | 11.68 ± 0.14 | 2.63 ± 0.36 |
| $H2$ | 1.593 | 0.053 | 11.78 ± 0.19 | 2.41 ± 0.46 |
| $H$ | 1.660 | 0.330 | 11.93 ± 0.14 | 1.95 ± 0.27 |
| $H3$ | 1.667 | 0.056 | 11.65 ± 0.19 | 2.30 ± 0.44 |
| $K1$ | 2.110 | 0.105 | 11.56 ± 0.09 | 1.09 ± 0.10 |
| $H_2$ 1−0 | 2.124 | 0.026 | 11.39 ± 0.14 | 1.23 ± 0.17 |
| $K_s$ | 2.180 | 0.350 | 11.53 ± 0.07 | 1.03 ± 0.07 |
| $K2$ | 2.251 | 0.112 | 11.29 ± 0.10 | 1.08 ± 0.10 |
| $L'$ | 3.800 | 0.620 | 11.05 ± 0.18 | 0.19 ± 0.04 |

**Notes.** [(a)] Full width at half maximum.

[4] http://www.eso.org/observing/etc/bin/gen/form?INS.MODE=swspectr+INS.NAME=SKYCALC.

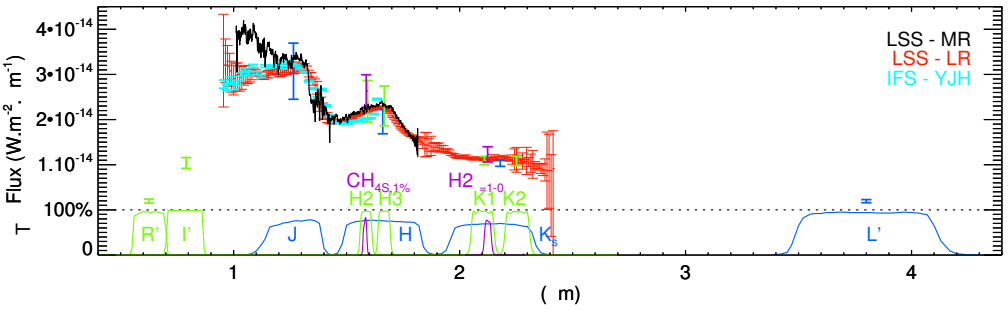


**Fig. 10.** Spectral energy distribution of PZ Tel B. The photometric data from SPHERE, NaCo, and NICI are indicated in light green, blue, and purple, respectively, along with the transmission curves of the associated filters.

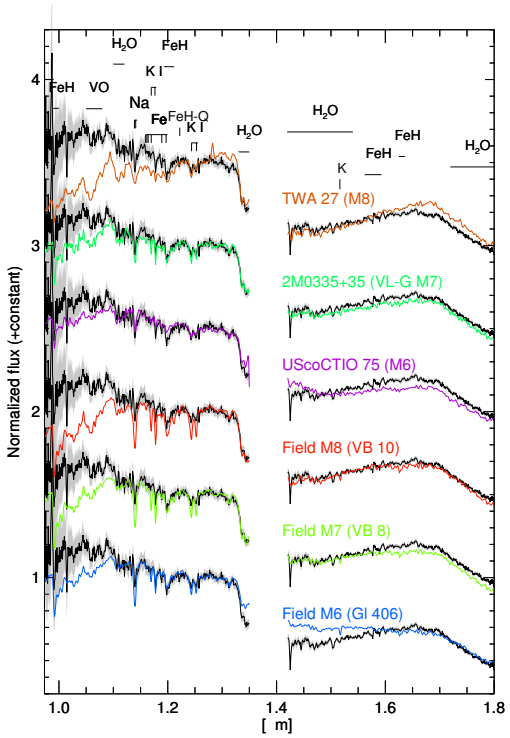


**Fig. 11.** Comparison of the MRS spectrum of PZ Tel B to those of field and young M6−M8 dwarfs.

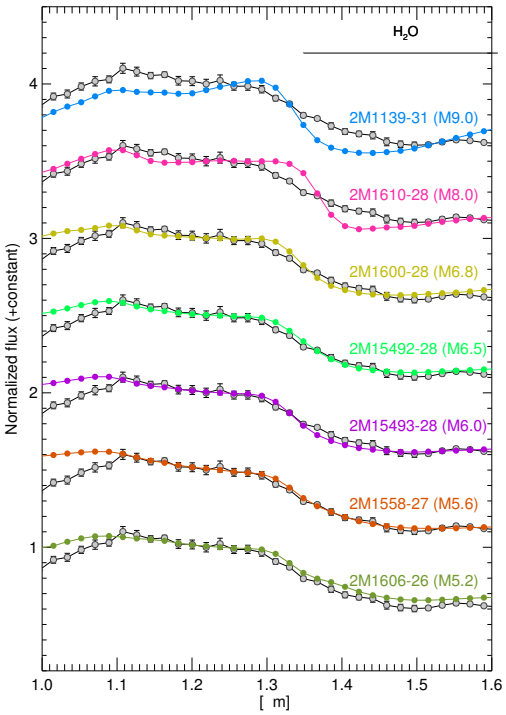


**Fig. 12.** Comparison of HD 1160 B IFS spectrum to the spectra of Upper Scorpius members (Dawson et al. 2014) and to 2MASS J11395113-3159214 (TWA 26).

converted to fluxes using the flux-calibrated spectrum of Vega, the model of the atmospheric transmission, and the corresponding filter passbands. The results are summarized in Table 9.

The SED of PZ Tel B is shown in Fig. 10. The IRDIS and NICI narrow-band photometry is in good agrement with the flux level of the LSS spectra. The figure highlights the excess of flux of the medium-resolution long-slit spectrum at the shortest wavelengths (Sect. 3.3.2). The IFS spectrum of the companion reproduces the features of the LRS spectrum quite well, although its slope seems to be flatter in the *H* band. We decided not to use this spectrum since it is superceded by the LRS spectrum.

### 5.2. Empirical study

The normalized LRS spectrum of PZ Tel B was compared to the low-resolution spectra of M, L, and T standard dwarfs of the SpeXPrism library (Burgasser 2014). The evolution of the $\chi^2$ with the spectral type indicates that the companion spectral type is in the M6−M8 range. We find a best match for the field M8 standard VB10 (van Biesbroeck 1961). In the bottom part of Fig. 11 we compare the MRS spectrum of the companion to those of M6−M8 field dwarf spectra from the SpeXPrism library. Then, we add in the top part of Fig. 11 a comparison to the spectra of the young M8 dwarf TWA 27 (TWA member − ∼8 Myr, Gizis 2002; Allers & Liu 2013), of the low-gravity dwarf 2MASS J03350208+2342356 (classified as M7 in the NIR, Gizis et al. 2000; Allers & Liu 2013), and of the M6 Upper Scorpius (3−11 Myr) member UScoCTIO 75 (Ardila et al. 2000; Allers & Liu 2013, 2MASS J16003023-2334457). The companion 1.2−1.8 $\mu$m pseudo-continuum is represented best by the pseudo-continuum of the M7 dwarfs. The gravity-sensitive 1.138 $\mu$m Na I doublet, as well as the K I lines (1.169, 1.177, 1.243, 1.253, and 1.516 $\mu$m) are weaker than the lines of field dwarfs and match those of young objects better. We therefore confirm the M7 ± 1 spectral type and the low surface gravity of the companion.

The IFS spectrum of HD 1160 B (Fig. 12) has a pseudo-continuum slope from 1 to 1.6 $\mu$m that is reproduced best by the SpeX (Rayner et al. 2003) spectra of M5.6−M6.8 Upper Sco members classified in the NIR (Dawson et al. 2014; Looper et al. 2007). Spectra of later or earlier-type objects than the interval quoted above do not reproduce the depth of the 1.33−1.5 $\mu$m water band, even if the companion spectrum has an absorption band

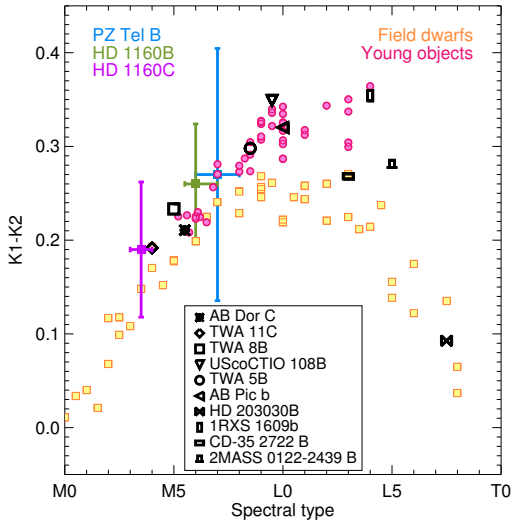


**Fig. 13.** Comparison of the $K1 - K2$ colors of PZ Tel B and of HD 1160 B and C to those of field dwarfs (yellow squares), young brown dwarfs at the M/L transition (pink circles), and companions to nearby young stars (symbols).

shortward of 1.1 $\mu$m that can only be reproduced by M8 dwarfs. We chose to assign a spectral type of M6.0$^{+1.0}_{-0.5}$ based on this comparison.

We report in Fig. 13 the $K1 - K2$ colors of HD 1160 B and C, and PZ Tel B and then compare them to those of standard field dwarfs synthesized from IRTF and NIRSPEC spectra (Cushing et al. 2005; Rayner et al. 2009; McLean et al. 2003). For HD 1160 C, we relied on the spectral type estimate derived by Nielsen et al. (2012) from its IRTF/SpeX NIR spectra. We added the synthetic colors of young companions computed from their spectra (Bonnefoy et al. 2014a; Allers & Liu 2013; Lafrenière et al. 2008; Wahhaj et al. 2011; Close et al. 2007; Bowler et al. 2013; Metchev & Hillenbrand 2006), low-gravity objects (Allers & Liu 2013) and Upper Sco dwarfs at the M/L transition (Dawson et al. 2014; Lodieu et al. 2008). For the latter, we followed the reclassification of the object proposed by Bonnefoy et al. (2014a). The remaining young and/or low-gravity objects were all classified at NIR wavelengths. The location of PZ Tel B and HD 1160 B in these diagrams is consistent with their spectral type derivation based on the NIR spectra. The slight offset with respect to the sequence of field dwarfs may be due to the reduced collision-induced absorption of $H_2$, so that the spectrum in the $K$ band is more curved. We conclude that the photometry of PZ Tel B and HD 1160 B is consistent with the spectral type derived from the NIR spectra. The $K1-K2$ color can be used with $YJH$-band low-resolution spectra to identify young L-type companions, provided that a high quality photometry (errors ≤0.05 mag) can be extracted from each IRDIS channel.

### 5.3. Synthetic spectra

We first compared the SED of PZ Tel B and HD 1160 B and C to those of synthetic spectra from the 2013 release of the BT-Settl[5] models (Allard et al. 2012). We also considered the restrained grid of synthetic spectra corresponding to the 2014 release of these models (Allard et al., in prep.), as well as the grid of DRIFT-PHOENIX models (Helling et al. 2008). The range of parameters for each model grid is summarized in Table 10. The BT-Settl14 models consider two $\alpha$-element enrichments. The DRIFT-PHOENIX and BT-Settl13 models allow us to explore the effect of the metallicity on the emergent spectra.

*PZ Tel B.* We compared the $I'$ and $R'$ (ZIMPOL), $L'$-band photometry, and LRS spectrum of PZ Tel B jointly to the three grids of synthetic spectra (hereafter version 1). We also considered an alternative version of the SED (version 2) made of the MRS spectrum longward of 1.1 $\mu$m (not affected by the flux excess) the $I'$ and $R'$ photometry, and the photometry longward of 2 $\mu$m. We used the $G'$ goodness-of-fit indicators to identify the best-fitting template. The fitting procedure is described in Cushing et al. (2008) and Vigan et al. (2016). The normalization factor used to fit the predicted surface flux onto the measured fluxes of the companion can be expressed as $(R/d)^2$ with $R$ and $d$ the source radius and the distance. Assuming the HIPPARCOS distance (51.5 pc, van Leeuwen 2007), we were therefore able to derive a radius estimate for the companion for each fitting solution. The atmospheric parameters, $G'$ values, radii, and Monte-Carlo $f_{MC}$ test of the fit robustness (see Cushing et al. 2008, and Vigan et al. 2016) for the companion and each model grid are reported in Table 11. The best-fitting solutions are shown in Figs. 14; and 15. The three most probable (highest $f_{MC}$) solutions, as well as the solution found with a $\chi^2$ test, were compared visually and discarded if necessary. We derived $T_{\rm eff}$ = 2700 ± 100 K from the models. They also indicate that the companion has a reduced surface gravity (≤4.5 dex). The comparison to the models shows that the LRS spectrum lacks fluxes in the $J$ band. The MRS spectrum is represented better by the models at these wavelengths. The imperfect fit of the optical photometry may be related to non-reproducibilities of the models in the red-optical domain (Bonnefoy et al. 2014a). The log($g$) agrees with the value found by Schmidt et al. (2014). The higher $T_{\rm eff}$ found here may be linked to the reduced water-band absorptions found in our spectra (SINFONI, SPHERE) with respect to the spectrum extracted by Schmidt et al. (2014), to the extended wavelength coverage, and/or to our different fitting method (reddening considered to be negligible here). The existence of best-fitting solutions for solar and subsolar metallicities (Table 11) indicates that this parameter could not be constrained.

*HD 1160 B.* We used the same procedure to compare the $K1$, $K2$ (SPHERE), $L'$ (NaCo) band photometry of HD 1160 B, and the IFS spectrum of the companion to the models. The synthetic spectra were first degraded to the IFS resolution[6] before the average flux into each IFS channel and filter passband was computed. We did not intend to repeat the analysis for HD 1160 C since its temperature was already accurately determined semi-empirically from its NIR spectrum by Nielsen et al. (2012) and spectral type to $T_{\rm eff}$ conversion scales. We found a $T_{\rm eff}$ = 3000 ± 100 K for HD 1160 B (Fig. 16 and Table 11). This agrees well with the $T_{\rm eff} = 2990^{+70}_{-110}$ K that can be derived from spectral type and the conversion scale of Luhman et al. (2003). The surface gravity could not be constrained with the presently available data. At low spectral resolutions like for the IFS data used in the fit ($R \sim 30$), a good indicator for the surface gravity of substellar objects is the spectral shape in the ~1.5−1.8 $\mu$m range (see, e.g., Barman et al. 2011; Chilcote et al. 2015), but

[5] "BT" refers to the source of water vapor line list used in these models (Barber et al. 2006) and "Settl" to models accounting for dust formation via a parameter-free cloud model (Rossow 1978).

[6] The flux values corresponding to the first and last two channels of IFS were removed from the fit since they appeared to be affected by systematic uncertainties not well accounted for in our error bars.

**Table 10.** Characteristics of the atmospheric model grids adjusted on the full SED of the substellar companions.

| Model name | $T_{\rm eff}$ (K) | $\Delta T_{\rm eff}$ (K) | $\log(g)$ (dex) | $\Delta\log(g)$ (dex) | [M/H] (dex) | $[\alpha]$ (dex) |
|---|---|---|---|---|---|---|
| BT-Settl13 | 400−3500 | 100 | 3.5−5.5 | 0.5 | 0.0 | 0.0 |
| BT-Settl13 | 800−3000 | 100 | 4.5−5.5 | 0.5 | +0.5 | 0.0 |
| BT-Settl13 | 1100−3000 | 100 | 3.5−6.0 | 0.5 | −0.5 | 0.2 |
| BT-Settl14 | 500−3000 | 50 | 3.5−5.5 | 0.5 | 0.0 | 0.0 |
| BT-Settl14 | 500−2800 | 100 | 4.0−5.5 | 0.5 | 0.0 | 0.3 |
| DRIFT-PHOENIX | 1500−3100 | 100 | 3.0−6.0 | 0.5 | −0.5, 0, +0.5 | 0.0 |

**Table 11.** Fitting solutions with the highest $f_{\rm MC}$ values for HD 1160 B and PZ Tel B SED and the three sets of atmospheric models using the $G'$ goodness-of-fit indicator.

| Object | Model | $T_{\rm eff}$ (K) | $\log(g)$ (dex) | [M/H] (dex) | $[\alpha]$ (dex) | $R$ ($R_{\rm J}$) | $G'$ | $f_{\rm MC}$ |
|---|---|---|---|---|---|---|---|---|
| HD 1160 B | BT-Settl14 | 3000 | 5.5 | – | 0.0 | 1.61 | 6.21 | 0.98 |
| | BT-Settl13 | 3000 | 6.0 | −0.5 | 0.2 | 1.64 | 3.75 | 0.22 |
| | DRIFT-PHOENIX | 2900 | 6.0 | −0.5 | – | 1.75 | 4.18 | 0.24 |
| PZ Tel B − v1 | BT-Settl14 | 2700 | 4.5 | – | 0.0 | 2.50 | 10.30 | 0.30 |
| | BT-Settl13 | 2700 | 4.0 | 0.0 | 0.0 | 2.61 | 7.61 | 0.30 |
| | DRIFT-PHOENIX | 2600 | 3.5 | −0.5 | – | 2.80 | 12.70 | 0.19 |
| PZ Tel B − v2 | BT-Settl14 | 2700 | 5.0 | – | 0.3 | 2.57 | 1.84 | 0.81 |
| | BT-Settl13 | 2600 | 3.5 | 0.0 | 0.0 | 2.86 | 1.88 | 0.16 |
| | DRIFT-PHOENIX | 2600 | 3.5 | 0.0 | – | 2.88 | 3.68 | 0.20 |

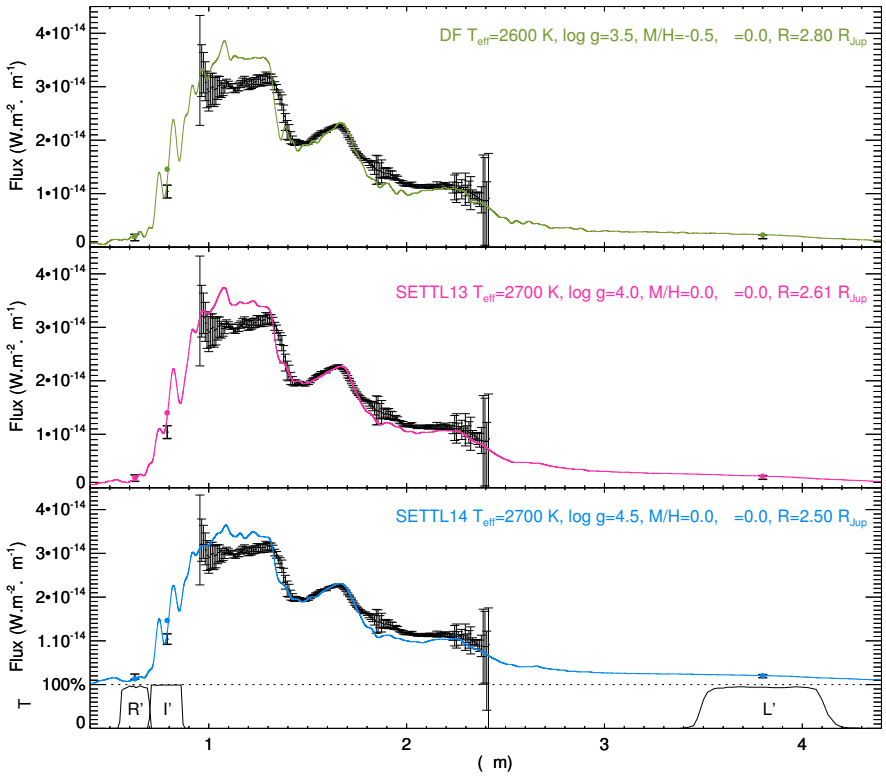


**Fig. 14.** First version of the PZ Tel B SED (black) compared to best-fitting synthetic spectra for three atmospheric models (see text).

this spectral range is outside the IFS coverage. Follow-up observations with the LSS mode of IRDIS will allow us to cover the full range of the $H$ band and to constrain the surface gravity of HD 1160 B (Fig. 16). The BT-Settl13 and DRIFT-PHOENIX grids point toward a subsolar metallicity for the companion. Additional medium-resolution spectra of the companion would be needed to confirm this point.

### 5.4. Revised masses

We used the new estimated temperatures of PZ Tel B and HD 1160 B to revise previous mass estimates.

*PZ Tel B.* The $T_{\rm eff}$ of PZ Tel B corresponds to a mass of $M = 45^{+9}_{-7}$ $M_J$ using Baraffe et al. (2015) "hot-start" evolutionary tracks. These tracks are based on the interior models of

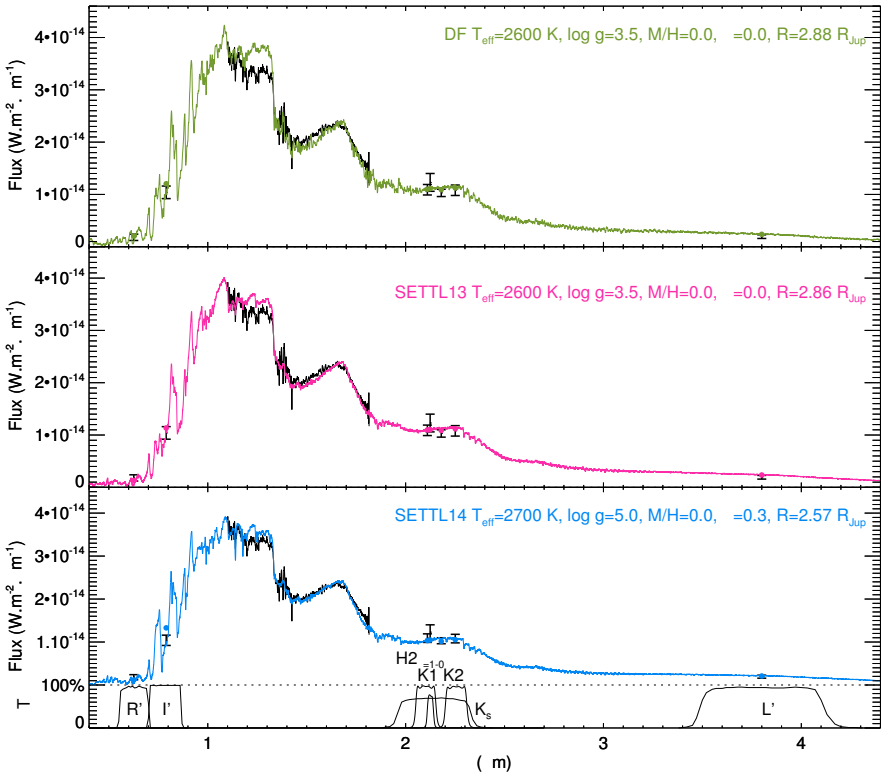


**Fig. 15.** Same as Fig. 14 but for the second version of the SED of PZ Tel B.

Baraffe et al. (1998) and use the BT-Settl14 models as boundary limits. We caution that the tracks do not explore the impact of the initial conditions on the mass predictions due to the lack of "cold-start" and "warm-start" evolutionary models (e.g., Marley et al. 2007; Spiegel & Burrows 2012) in the brown-dwarf mass range. We assumed a mean system age of $24 \pm 2$ Myr (Jenkins et al. 2012), which agrees with the most recent estimates for the age of the $\beta$ Pictoris moving group (Binks & Jeffries 2014; Malo et al. 2014; Mamajek & Bell 2014). We used the mean contrast in the $K_s$ band ($5.26 \pm 0.06$ mag) from Mugrauer et al. (2012), the $K$-band magnitude of the star reported in Sect. 4.1, and a $BC_K = 3.05 \pm 0.10$ mag from Liu et al. (2010a) to derive $\log(L/L_\odot) = -2.51 \pm 0.10$ dex. This corresponds to a mass of $M = 59^{+13}_{-8}\,M_J$ according to the evolutionary tracks of Baraffe et al. (2015). These mass predictions are consistent one to each other within the error bars. They fall above those reported in Biller et al. (2010) and Schmidt et al. (2014), because of the older system age adopted here. We reach similar conclusions comparing the NaCo $L'$ band magnitude to the Baraffe et al. (1998) tracks.

*HD 1160 C.* We used the $T_{\rm eff}$ vs. spectral type conversion scale of young objects from Pecaut & Mamajek (2013) and the spectral type determined by Nielsen et al. (2012) to re-estimate a $T_{\rm eff} = 3260 \pm 100$ K for HD 1160 C. The conversion scale valid for old objects (Pecaut & Mamajek 2013) yields close results ($T_{\rm eff} = 3300 \pm 100$ K). Nielsen et al. (2012) estimate that HD 1160 C has a $BC_K = 2.72 \pm 0.06$ mag using the estimated spectral type of the companion and the relations tabulated in Golimowski et al. (2004). We preferred to use the relations of Pecaut & Mamajek (2013) instead of those of Golimowski et al. (2004) because the latter are not valid for objects later than M6. The NICI $J$-band photometry of the system appears to be at odds with the $J$-band photometry of HD 1160 B derived from SPHERE IFS data (see below). Nevertheless, the NICI $K_s$-band photometry of both companions agree with the SPHERE IRDIS photometry in the $K12$ filter pair. Consequently, we used the NICI $K_s$-band photometry of HD 1160 C, as well as the bolometric corrections reported in Pecaut & Mamajek (2013) to find $\log(L/L_\odot) = -2.05 \pm 0.06$ dex.

*HD 1160 B.* Nielsen et al. (2012) show that HD 1160 B has redder $J - K_s$ colors than the sequence of field dwarfs. Using the extracted IFS spectrum of the companion and the NICI filter passbands, we instead found $\Delta J = 7.43 \pm 0.03$ mag and $M_J = 9.53 \pm 0.11$ mag. We assessed that both the $K1$ and $K2$ photometry of the companion match $M_{K_s} = 8.88 \pm 0.12$ mag using the NICI and SPHERE filter passbands and spectra of Upper Sco M5.5−M7 dwarfs (Dawson et al. 2014). The $K$-band photometry is consistent within error bars with the value derived in Nielsen et al. (2012). The revised color $J - K = 0.50 \pm 0.07$ mag is bluer than expected ($J - K = 0.90 \pm 0.07$ mag) for a $\mathrm{M6.0}^{+1.0}_{-0.5}$ dwarf. This may be due to the methods used to estimate the new photometry. However, such blue colors correspond to those of mid-M subdwarfs and could thus be due to subsolar metallicity, as already discussed in Sect. 5.3. We relied on the SPHERE $K_s$-band photometry in the following. We estimated a $BC_K = 3.00^{+0.05}_{-0.01}$ mag for HD 1160 B using the corrections from Liu et al. (2010a) and the spectral type estimate from Sect. 5.2. We derived $\log(L/L_\odot) = -2.81 \pm 0.10$ dex.

We compare HD 1160 B and C $T_{\rm eff}$ and luminosities to Baraffe et al. (2015) evolutionary tracks in Fig. 17. Both companions fall marginally (within $2\sigma$) onto the 100−120 Myr isochrone. HD 1160 B lies at the substellar boundary. In comparison, PZ Tel B still falls onto the 20 Myr isochone, in agreement with the host star age. We reach similar conclusions using the Baraffe et al. (1998) models and the $L'$-band magnitudes[7] of the objects (Sect. 3.5).

[7] The predictions of Baraffe et al. (2015) models for the NaCo filter set were not available at the time of the submission of this article.

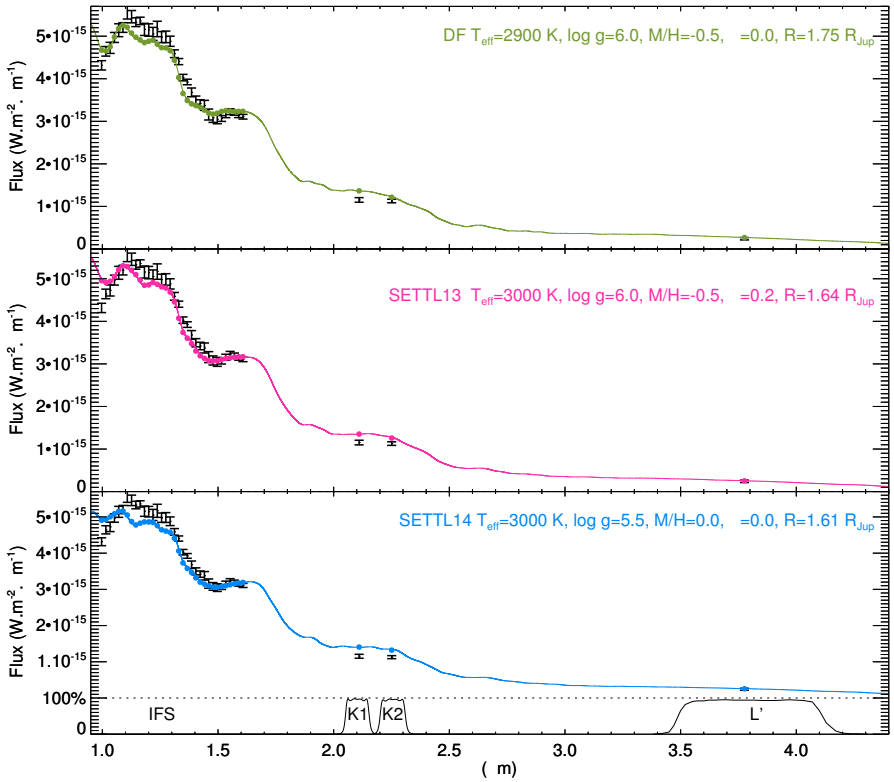


**Fig. 16.** Comparison of the SED of HD 1160 B (black) to best-fitting synthetic spectra for three atmospheric models (see text).

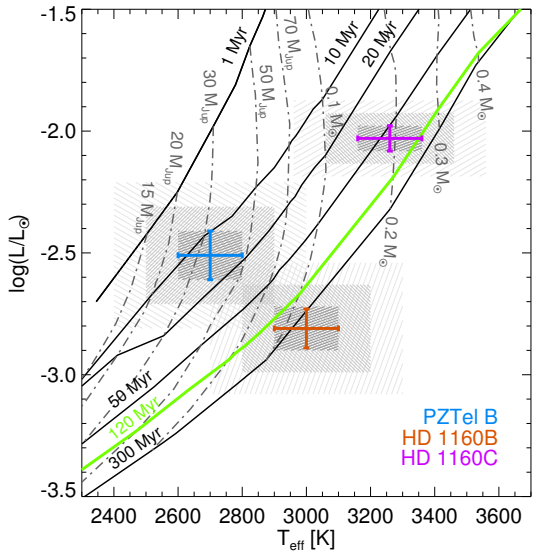


**Fig. 17.** Location of the companions with respect to the predictions of the Baraffe et al. (2015) models. The concentric hatched areas show the 1, 2, and 3$\sigma$ values for the estimated parameters.

This questions previous age estimates of HD 1160 A[8]. The age of the star is difficult to estimate because of the small number of reliable age indicators for this target. Nielsen et al. (2012) argue that HD 1160 A cannot be older than 300 Myr because of the expected main-sequence lifetime of an A0 star (Siess et al. 2000). The kinematics of HD 1160 are still compatible (2.8$\sigma$ in $U$, <1$\sigma$ in $V$, and 2.3$\sigma$ in $W$) with the Octans-Near association (Zuckerman et al. 2013), for which Murphy & Lawson (2015) estimate a 30−40 Myr lithium age. Nielsen et al. (2012) show that the location of HD 1160 A and C in HR diagrams is consistent with both the young associations and the Pleiades, but indicates a younger age than the Pleiades. Nevertheless, this analysis relied on the $J$-band photometry of HD 1160 C, which may be biased. The revised photometry of the system and our analysis of the spectro-photometry instead suggest that the system has a subsolar metallicity. In that case, HD 1160 A falls onto the 10−300 Myr isochrones in HR diagrams (Nielsen et al. 2012). Using the constraints from the kinematics and the isochrones, we considered an age of $100^{+200}_{-70}$ Myr for the system in the following.

For the mass of HD 1160 C, we estimate $M_C = 205^{+72}_{-51}$ and $244^{+113}_{-70}$ $M_J$ from its $T_{\rm eff}$ and bolometric luminosity, respectively, assuming the Baraffe et al. (2015) evolutionary models. For HD 1160 B, estimates are $M_B = 107^{+59}_{-38}$ and $79^{+65}_{-40}$ $M_J$, respectively. The masses for HD 1160 B are revised to higher values with respect to the estimate of $33^{+12}_{-9}$ derived by Nielsen et al. (2012), because of a combination of a brighter $J$-band magnitude estimate (by 1.22 mag) and of an age range estimate covering older values (up to 300 Myr against 100 Myr). The larger error bars compared to the estimate in Nielsen et al. (2012) stem from the larger uncertainties in our estimate of the system age. When considering the youngest possible ages, the masses fall in the substellar regime. They marginally agree with those of Nielsen et al. (2012). Nonetheless, we cannot exclude that HD 1160 B is a low-mass star for the oldest possible ages. The radius and $T_{\rm eff}$ of HD 1160 B estimated from the synthetic spectra (Sect. 5.3) are notably well reproduced for ages ≥100 Myr. We note that the new mass estimates of both companions agree with the predictions of a formation scenario by disk instability in a disk of mass half of the stellar mass (see Fig. C.1 in Bonnefoy et al. 2014b).

[8] We note that for the statistical study of the NICI survey of young B and A stars, Nielsen et al. (2013) derive an older age of 92 Myr, with 68% confidence between 36 and 178 Myr, based on a Bayesian analysis.

**Table 12.** Masses for PZ Tel B and HD 1160 BC derived in this work compared to literature estimates.

| Parameter | PZ Tel B ($M_J$) | HD 1160 B ($M_J$) | HD 1160 C ($M_J$) |
|---|---|---|---|
| $\log(L/L_\odot)$ | $59^{+13}_{-8}$ | $79^{+65}_{-40}$ | $244^{+113}_{-70}$ |
| $T_{\rm eff}$ | $45^{+9}_{-7}$ | $107^{+59}_{-38}$ | $205^{+72}_{-51}$ |
| Literature | $36 \pm 6^a$ | $33^{+12b}_{-9}$ | $220^{+30b}_{-40}$ |

**References.** [(a)] Biller et al. (2010). [(b)] Nielsen et al. (2012).

Given the new mass estimates in Table 12, PZ Tel B and potentially HD 1160 B can be added to the scarce population of companions with mass ratios with respect to their host star below 0.1 (Raghavan et al. 2010). Recently, such low-mass companions have been reported around intermediate-mass stars in the Sco-Cen stellar association (Hinkley et al. 2015b) and the F-type star HD 984 (Meshkat et al. 2015). The observed statistical properties (e.g., mass ratio, eccentricity) of these objects can be compared to the predictions of formation scenarios (e.g., Bate 2009; Raghavan et al. 2010). For both PZ Tel and HD 1160 systems, a formation mechanism based on the collapse and the fragmentation of a dense molecular cloud seems plausible. Gravitational instabilities in a disk may also explain the formation of the companions in both systems, provided subsequent dynamical interactions excited the measured eccentricity for PZ Tel B and early fragmentation in the disk occurred for the HD 1160 system to meet the requirement of a high mass for the disk (see above and Fig. C.1 in Bonnefoy et al. 2014b).

## 6. Constraints on the orbit of PZ Tel B

In Ginski et al. (2014), it was noted that possible deceleration of the companion is detectable in the 2012 VLT/NaCo data. This was done by comparing its relative astrometric position in 2012 to the position obtained by linear fitting of the data taken between 2009 and 2011. The deviation from simple linear motion was on the $2\sigma$ level in position angle. In Fig. 18, we show the previous relative astrometric measurements of the system from Mugrauer et al. (2012) and Ginski et al. (2014), along with the same linear fit and our new SPHERE/IRDIS measurements. The IRDIS measurements are clearly deviant from the linear motion fit in position angle ($9.4\sigma$). In addition, we also observe a highly significant[9] deviation from simple linear motion in separation ($25.5\sigma$). It is in principle possible that a small systematic offset exists between the NaCo and IRDIS data since the reference fields used for astrometric calibration are different. However, given that the current trend in PA was already detected in the NaCo data and that the significance of the detected deceleration is very high, we conclude that the companion is decelerating, which is consistent with it moving toward apastron[10].

We then used the two astrometric measurements taken with SPHERE/IRDIS to further constrain the orbital elements of the system taking the previous astrometric measurements with VLT/NaCo presented in Mugrauer et al. (2012) and Ginski et al. (2014) into account. For this purpose, we considered a least-squares Monte Carlo (LSMC) fitting technique, which was

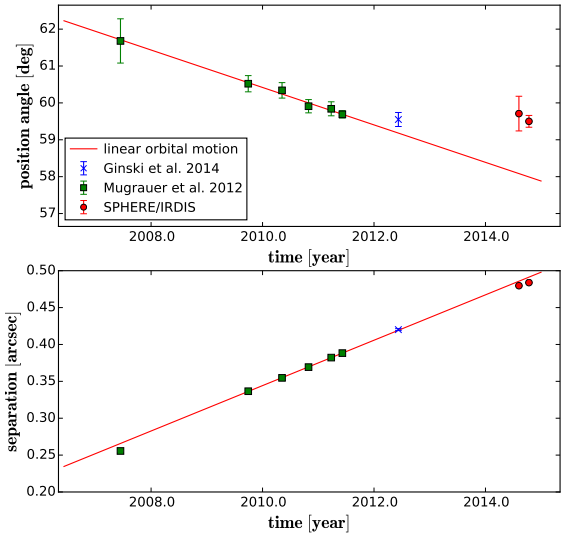


**Fig. 18.** Relative astrometric measurements of the PZ Tel system. The linear motion fit (red solid line) was computed by taking only the data points between 2009 and 2011 into account.

presented in detail in Ginski et al. (2013). The fitting algorithm created $5 \times 10^6$ random sets of orbit parameters, which were drawn from uniform distributions, without considering the astrometric data. These parameter sets were then used as starting points for a least-squares minimization. To constrain the parameter space, we fixed the system mass to 1.2 $M_\odot$ as done in Ginski et al. (2014). We also set an upper limit to the semi-major axis assuming that the system is stable against disruptions in the galactic disk. To estimate this value, we utilized the relation $a_{\rm max}[{\rm au}] = 1000\, M_{\rm tot}/M_\odot$ as given in Close et al. (2003) (where $M_{\rm tot}$ is the total system mass in solar masses, and $a_{\rm max}$ the maximum stable semi-major axis). This put an upper limit on the semi-major axis of 23.3″ (~1200 au). In addition, we limited our orbit fitting to longitudes of the ascending node $\Omega$ between 0 and 180°, since no precise radial velocity measurements of the companion are available.

The results of the fitting procedure are displayed in Fig. 19. Shown are all orbit solutions with $\chi^2_{\rm red} \leq 2$. We also show the three best-fitting orbits in Fig. 20, along with their corresponding parameters in Table 13. Compared to the previous analysis of the system in Ginski et al. (2014), the possible parameter space for orbital fitting with the astrometric measurements can be constrained somewhat further. We find a lower limit for the semi-major axis of 0.52″ (previously 0.38″) and a corresponding lower limit for the eccentricity of 0.66 (previously 0.62). Orbit periods range between 126.6 and 37938.3 yr. The results of our new analysis show two distinguishable branches for orbits considering semi-major axis and eccentricity, which are visible in the top lefthand panel of Fig. 19. One branch shows a strongly increasing semi-major axis with increasing eccentricity. The other branch exhibits small semi-major axes (≤1.1″) even for eccentricities up to ~0.9 and then also rises quickly toward large semi-major axes. In the first case, the orbit inclination is well constrained between ~91° and 94°, while in the latter the inclination rises with increasing eccentricities to values of up to 100° until eccentricities of up to 0.95 and then even higher inclinations of up to 153.4°. With further monitoring in the next few years, it might well be possible to exclude or confirm especially short period orbits in this second branch.

It is also useful to look into possible orbit constraints for the less extreme eccentricity cases with $e \leq 0.9$. If indeed the orbit

[9] Error bars in Fig. 18 are much smaller than the displayed markers.

[10] It should be noted that previously deceleration of the companion was detected by Mugrauer et al. (2010) between the earliest 2007 observation epoch and the later 2009 epoch. This is also visible in Fig. 18 as a deviation of this epoch from the linear motion fit.

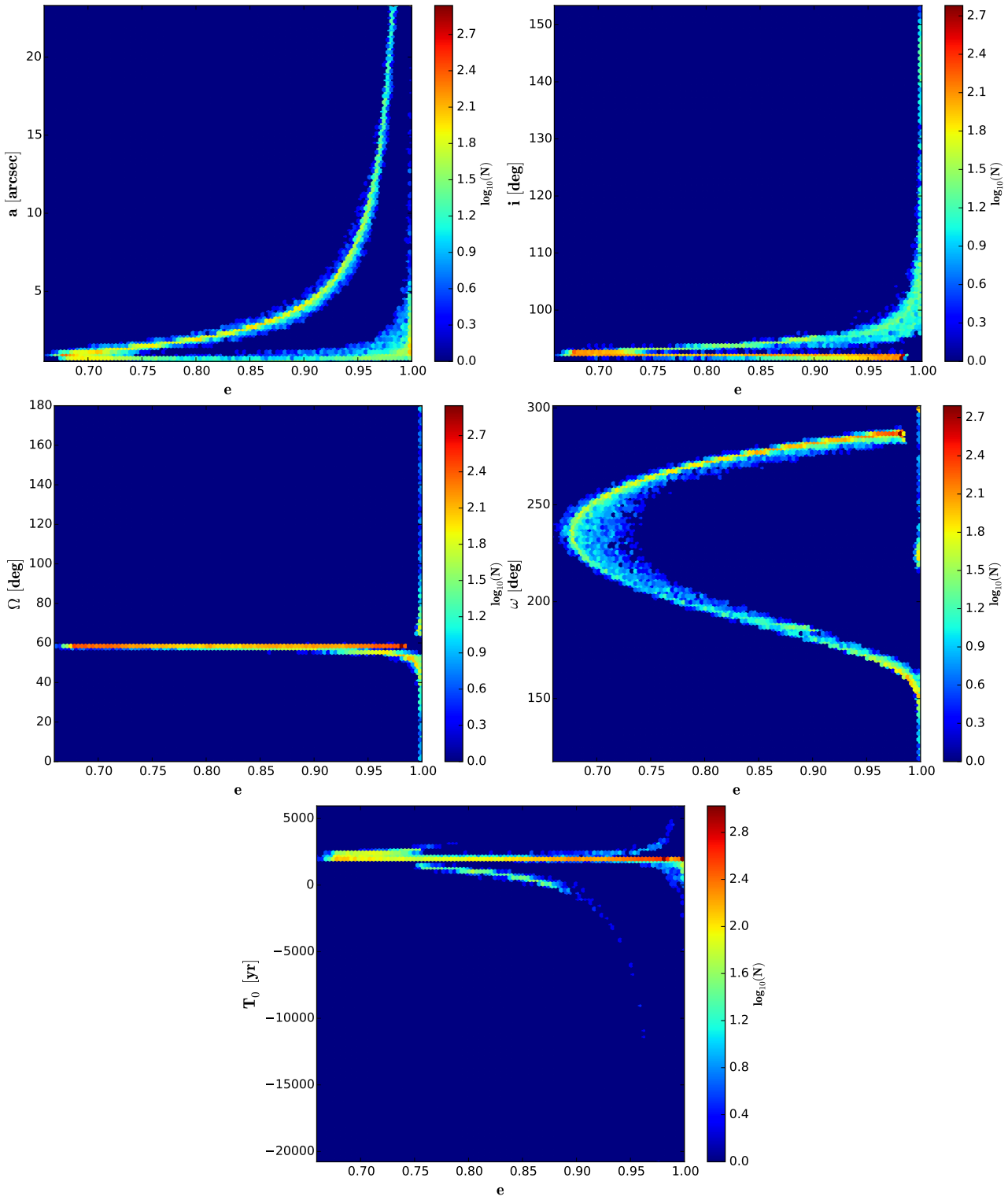


**Fig. 19.** Orbital elements as function of eccentricity for all solutions with $\chi^2_{\rm red} \leq 2$ out of 5 000 000 runs of our LSMC fit of the PZ Tel B astrometric data. *From left to right and from top to bottom* are represented the semi-major axis, inclination, longitude of the ascending node, argument of periastron, and time at periastron passage. Logarithmic density of solutions is indicated by color.

eccentricity were not higher than this value, the orbit would already be well constrained. In particular, the inclination would be limited to values between 91.0° and 96.1°, and the longitude of the ascending node would lie between 55.1° and 59.1° (with a possible change in direction of +180° depending on radial velocity). In this scenario and given that the host star is seen almost from its equator (Sect. 4.4), the PZ Tel system is close to a configuration with spin-orbit alignment. In addition, semi-major axes would lie between 0.52″ and 4.72″, i.e. orbital periods between 126.9 and 3455.9 yr.

More than two-thirds of all orbit solutions (72.6%) have a time of the periastron passage between 1994 and 2005. This is very consistent with the non-detection of the companion in VLT/NaCo images of epoch 2003.55 as reported in

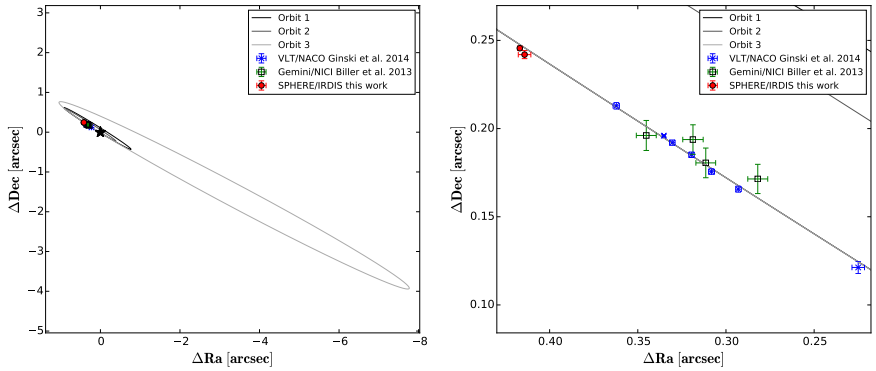


**Fig. 20.** Top 3 best-fitting orbits out of 5 000 000 runs of our LSMC fit of the PZ Tel B astrometric data. Solid lines represent the apparent orbits. The *right panel* is zoomed in on the data points. The corresponding orbit elements are listed in Table 13. We show the data points taken with VLT/NaCo as given in Ginski et al. (2014; blue crosses), as well as the data points taken with Gemini/NICI given in Biller et al. (2013; empty green boxes), together with our SPHERE/IRDIS measurements (red circles). For the orbit fitting, only the VLT/NaCo and SPHERE/IRDIS data points were considered.

**Table 13.** Parameters and $\chi^2_{\rm red}$ of the best-fitting orbits for PZ Tel B shown in Fig. 20.

| Orbital solution | 1 | 2 | 3 |
|---|---|---|---|
| $a$ [″] | 1.504 | 0.951 | 13.409 |
| $e$ | 0.755 | 0.686 | 0.969 |
| $P$ [yr] | 622.2 | 313.1 | 16563.3 |
| $i$ [°] | 92.05 | 92.34 | 91.83 |
| $\Omega$ [°] | 58.43 | 58.25 | 58.58 |
| $\omega$ [°] | 264.38 | 241.99 | 286.54 |
| $T_0$ [yr] | 2000.0 | 1997.5 | 2003.8 |
| $\chi^2_{\rm red}$ | 1.220 | 1.220 | 1.223 |

**Notes.** The notations for the orbit elements refer to the semi-major axis, eccentricity, orbital period, inclination, longitude of the ascending node, argument of periastron, and time of periastron passage.

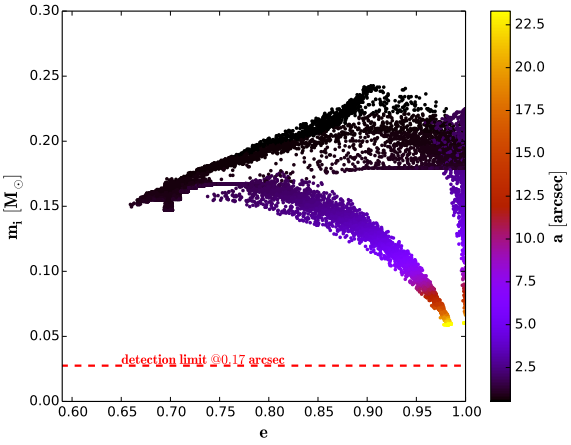


**Fig. 21.** Minimum mass of an unseen inner companion that would cause a false positive eccentricity signal in the relative astrometry of PZ Tel A and B by astrometric displacement of PZ Tel A due to their common orbit around their center of mass. The minimum mass is shown for all the recovered orbits with $\chi^2_{\rm red} \leq 2$ (see text). We also indicate the minimum mass of a putative inner companion detected in the IRDIS $K2$-band images at the angular separation at which it would need to reside.

Masciadri et al. (2005). In fact, all our recovered orbits exhibit a separation smaller than 0.16″ for this observation epoch, which is the minimum separation for which a companion as massive as PZ Tel B would have been detected in the corresponding study.

The best-fitting orbits that we recovered are shown in Fig. 20 with the corresponding orbit elements listed in Table 13. Compared to previous studies, it is notable that with the SPHERE/IRDIS data points, the best-fitting orbits are less eccentric. Specifically, the previously best-fitting orbit for this system exhibited an eccentricity greater than 0.99, while in our new analysis the best-fitting orbit only exhibits an eccentricity of 0.755. This orbit configuration is much more likely to produce a long-term stable orbit than the high eccentricity case. In addition to the VLT measurements, we show astrometric data points obtained with Gemini/NICI by Biller et al. (2013) overplotted on our best-fitting orbits. They show a larger intrinsic scatter and also larger uncertainties compared to the considered VLT/NaCo and SPHERE/IRDIS measurements. However, they also agree with the best-fitting orbits within ~1.1$\sigma$.

In a recent study, Pearce et al. (2014) discuss the problems that additional undetected inner companions could cause for the orbit determination of known direct imaging companions. In particular, they point out that an inner companion on a much shorter period than the outer direct imaging companion would introduce an astrometric "wobble" to its host star, owing to their orbital motion around their common center of mass. This astrometric signal would then influence the relative astrometric measurements between the host star and the direct imaging companion. This could lead to apparent orbits derived from this relative astrometry that appear eccentric, while in fact the true orbit of the outer companion is circular or nearly circular.

To validate the high eccentricities found for the PZ Tel system, we used the formalism introduced in Pearce et al. (2014) and computed the minimum mass and distance of such a putative inner companion for each of our recovered orbit solutions[11]. We then compared these masses with the detection limits derived from our deep IRDIS $K2$-band images (Sect. 7). The results are shown in Fig. 21. In principle, inner companions with masses between ~0.06 and ~0.25 $M_\odot$ could cause a false positive eccentricity signal in case of the PZ Tel system. However, all of these putative companions would have been detected in our IRDIS images. Thus, we can conclude that the observed high eccentricities of PZ Tel B are genuine.

## 7. Constraints on putative additional companions

We discuss the constraints on putative additional companions in both PZ Tel and HD 1160 systems using the sensitivity of the IRDIS images in the $K12$ filter pair and in the IFS $YJH$ data sets. We present in Fig. 22 the detection limits for both IRDIS $K1$ and $K2$ images processed with TLOCI using ADI alone (Sect. 3.1). Figure 23 shows the detection limits measured in the IFS data analyzed with ADI using a PCA algorithm (Sect. 3.3.1). The PCA

[11] A similar computation for an exemplary orbit has already been done in Pearce et al. (2014); however, the results depend on the semi-major axis and eccentricity of the apparent orbits, thus it is sensible to repeat the calculation for all orbit solutions. The minimum mass is also a function of the maximum epoch difference of all astrometric data.

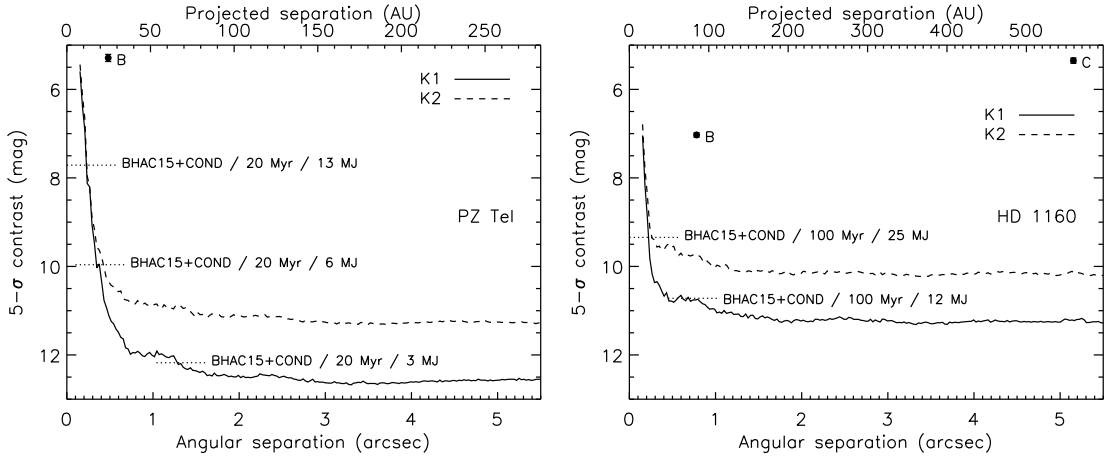


**Fig. 22.** SPHERE/IRDIS detection limits for the images in the $K12$ filter pair analyzed with TLOCI using ADI only for the systems PZ Tel (*left*) and HD 1160 (*right*). The mass limits are estimated from the atmospheric and evolutionary "hot-start" model BHAC15+COND (Baraffe et al. 2015). The relative magnitude of the companions and the mass predictions are derived for the $K1$ band.

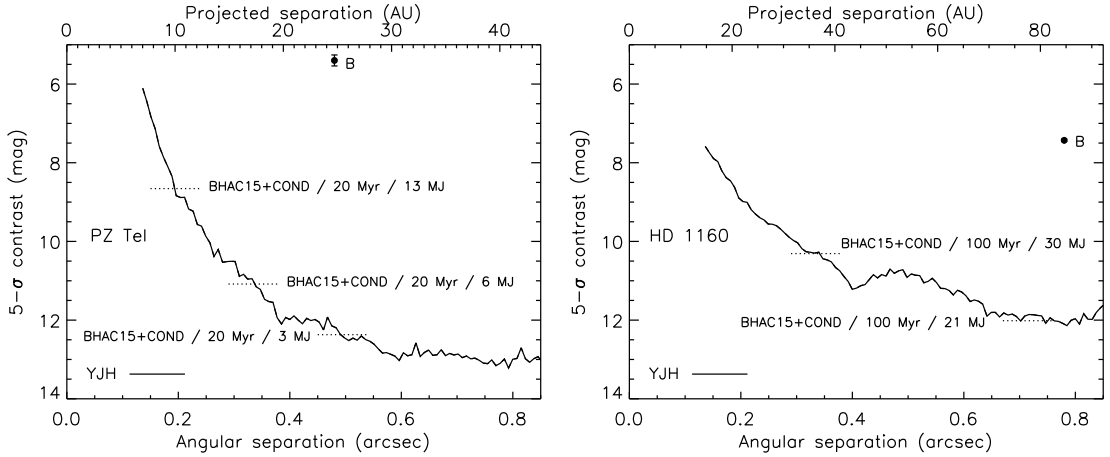


**Fig. 23.** SPHERE/IFS detection limits for the $YJH$ spectral data cubes analyzed with PCA using ADI only for the systems PZ Tel (*left*) and HD 1160 (*right*). The resulting spectral data cube was collapsed before the estimation of the detection limits. The mass limits are estimated from the atmospheric and evolutionary "hot-start" model BHAC15+COND (Baraffe et al. 2015). The plotted relative magnitude of the companions is in the $J$ band and the mass derived from model predictions in this band.

algorithm was applied to each spectral channel. The detection limits were measured in the collapsed PCA data cube. For deriving the mass limits, we used the predictions of the atmosphere and evolutionary "hot-start" model BHAC15+COND (Baraffe et al. 2015) derived in the IRDIS filters and the IFS bands.

Before analyzing the detection limits, we emphasize that the contrast performance shown in Figs. 22 and 23 is not representative of the SPHERE requirements (∼12.5−15 mag at 0.5−1″). We recall that the primary goals of the commissioning runs were to test and validate the instrument modes on sky. The IRDIFS_EXT observations used here are snapshots and cover small field rotations (Table 1). The short integration times and the relative faintness of PZ Tel and HD 1160 in the NIR bands (∼6−7 mag) are the main limiting factors to the contrast performance at large angular separations ($\gtrsim$1″), where the dominant source of noise is thermal background. The thermal background increases with wavelength, hence the poorer contrast performance observed for IRDIS in the $K2$ band with respect to the $K1$ band. The small field rotations limit the performance at small angular separations ($\lesssim$1″), because of the algorithm throughput that counterbalances the gain in contrast offered by the PSF subtraction.

For the PZ Tel system, the field rotation for the data is small (9°). Despite this, the IRDIS detection limits in the $K1$ filter allow brown dwarf companions ($M > 13\ M_J$) to be excluded outside 0.25″ and massive (>6 $M_J$) giant planet companions outside ∼0.4″. The IFS data are sensitive to brown dwarf companions outside 0.2″ and giant planets more massive than 3 $M_J$ beyond ∼0.5″. Detection limits on additional companions were presented in Mugrauer et al. (2010), Biller et al. (2013), Ginski et al. (2014) based on VLT/NaCo $K_s$-band images or Gemini/NICI broad-band data in the $H$ band[12]. We achieve contrasts with IRDIS in the $K1$ narrow-band filter deeper than the contrasts reported in Ginski et al. (2014) with NaCo in the $K_s$ broad-band filter at separations beyond ∼0.3″.

For the HD 1160 system, the data were obtained in better conditions (field rotation ∼18.5°). Nonetheless, the star is fainter in the NIR with respect to PZ Tel. Thus, the contrasts that we

[12] We note that Biller et al. (2010, 2013) derived detection limits combining ADI and dual-band differential imaging in narrow-band images in the $H$ band. Nevertheless, the detection limits do not account for the throughput of the dual-band differential imaging, because the latter depends on the assumed spectral properties for the companions.

achieve with IRDIS are higher in the speckle-limited regime and lower in the background-limited regime. The sensitivity to low-mass companions is worse with respect to PZ Tel because of the older age and farther distance of HD 1160. We can reject brown dwarf companions outside 0.25″ based on the IRDIS detection limits. The sensitivity of the IFS data allows us to exclude massive (>25 $M_J$) brown dwarf companions beyond ~0.5″. The contrasts that we measured for the IRDIS $K1$ narrow-band data are deeper than the contrasts in broad $H$ band presented in Nielsen et al. (2013)[13] at close-in separations (≲0.75″) and are more sensitive to putative additional low-mass companions.

## 8. Conclusions

We have presented first light results of the new planet finder VLT/SPHERE for the young systems PZ Tel and HD 1160. These data were analyzed with complementary literature and unpublished data from existing facilities (VLT/SINFONI, VLT/NaCo, Gemini/NICI, Keck/NIRC2) to provide new insight into both systems.

We first studied the short-term and long-term photometric variability of the host star PZ Tel A based on REM and literature data. The results for the rotational period agree with previous studies. We also estimated updated photometry for the star at optical and NIR wavelengths. We used the NIR updated photometry of the host star with optical and NIR spectrophotometry measured for the companion PZ Tel B to analyze the SED and physical characteristics of the latter. We confirmed a M7 ± 1 spectral type and a low surface gravity $\log(g) < 4.5$ dex, but found a higher effective temperature $T_{\rm eff} = 2700 \pm 100$ K. The metallicity could not be constrained. Assuming the stellar age of 24 ± 2 Myr suggested by Jenkins et al. (2012), we proposed a revised mass of PZ Tel B of $45^{+9}_{-7}$ $M_J$ based on its effective temperature and $59^{+13}_{-8}$ $M_J$ based on its bolometric luminosity. We used the new SPHERE/IRDIS astrometry to update the constraints on the orbital parameters of the companion. We confirmed its deceleration and the high eccentricity of its orbit $e > 0.66$. The deep SPHERE/IRDIS detection limits suggest that this high eccentricity is genuine and not induced by an unseen companion very close to the star. The time of periastron passage for more than 70% of the possible orbits is consistent with the non-detection of the companion in 2003 VLT/NaCo data (Masciadri et al. 2005). For eccentricities below 0.9, we constrain the inclination to nearly edge-on values (within ~6°) and the longitude of the ascending node to values in the range ~55–59°. Further astrometric monitoring in the coming years will provide upper limits on the orbital eccentricity. Based on "hot-start" evolutionary models, we were able to exclude brown dwarf companions ($M > 13$ $M_J$) outside 0.2″ and massive (>3 $M_J$) giant planet companions beyond ~0.5″.

For the HD 1160 system, we derived the first NIR spectral classification ($R \sim 30$) of HD 1160 B and found a spectral type $M6.0^{+1.0}_{-0.5}$. This spectral type is earlier than the estimate by Nielsen et al. (2012) based on the NICI photometry (L0 ± 2). The $J - K_s$ color derived from the SPHERE data agrees with the colors of field dwarfs, although it is slightly bluer with respect to dwarfs of the same spectral type. This could be a hint that there is subsolar metallicity for the companion. Medium-resolution spectroscopy is needed to confirm this point. We constrained the effective temperature of HD 1160 B to a value of 3000 ± 100 K but not its surface gravity. For HD 1160 C, we estimated $T_{\rm eff} = 3260 \pm 100$ K, which agrees with the results of Nielsen et al. (2012). The effective temperature and bolometric luminosity of HD 1160 B and C marginally agree (within $2\sigma$) with an age of 100–120 Myr, which corresponds to the upper limit of the range derived by Nielsen et al. (2012) ($50^{+50}_{-40}$ Myr). Assuming an age for the host star of $100^{+200}_{-70}$ Myr, we assessed a mass for HD 1160 B of $107^{+59}_{-38}$ $M_J$ (based on effective temperature) and $79^{+65}_{-40}$ $M_J$ (based on bolometric luminosity). For the lowest values in the age range, our mass estimates are in the substellar regime and marginally agree with the results of Nielsen et al. (2012). Nevertheless, the uncertainties on the system age do not allow us to exclude that HD 1160 B is a low-mass star. The corresponding mass estimates for HD 1160 C are $205^{+72}_{-51}$ $M_J$ and $244^{+113}_{-70}$ $M_J$, respectively. These estimates agree with the values reported in Nielsen et al. (2012), but have larger error bars due to the larger error bars adopted for the stellar age. Further astrometric follow-up of the system may reveal orbital motion for both companions thanks to the improved astrometric accuracy of the SPHERE measurements (<3 mas in separation and ≤0.2° for the parallactic angle) with respect to previous data (Nielsen et al. 2012). The SPHERE detection limits allow excluding brown dwarf companions outside 0.25″, assuming "hot-start" evolutionary models.

*Acknowledgements.* We thank the anonymous referee for a constructive report on the manuscript and Daniel Rouan for helpful suggestions. The authors are grateful to the Consortium and the ESO Paranal Staff for making SPHERE a reality. The authors warmly thank Andrea Bellini and Jay Anderson for kindly providing the catalog positions of the stars in the 47 Tuc field before their publication. We are also grateful to ESO for releasing the commissioning data for publication. A.-L.M., S.M., D.M., R.G., S.D., R.U.C., and A.Z. acknowledge support from the "Progetti Premiali" funding scheme of the Italian Ministry of Education, University, and Research. A.-L.M. thanks the MPIA for support during the last stages of this work. A.V., M.B., G.C., and D.M. acknowledge financial support from the French National Research Agency (ANR) through the GUEPARD project grant ANR10-BLANC0504-01, the CNRS-D2P PICS grant, and the Programmes Nationaux de Planétologie et de Physique Stellaire (PNP & PNPS). D.E. acknowledges the financial support of the Swiss National Science Fundation (SNSF) through the National Centre for Competence in Research "PlanetS". A.Z. acknowledges support from the Millennium Science Initiative (Chilean Ministry of Economy), through grant "Nucleus RC130007". This research has benefitted from the SpeX Prism Spectral Libraries, maintained by Adam Burgasser at http://pono.ucsd.edu/~adam/browndwarfs/spexprism. This research made use of the SIMBAD data base, as well as the VizieR catalog access tool, both operated at the CDS, Strasbourg, France. The original description of the VizieR service was published in Ochsenbein et al. (2000, A&AS, 143, 23). SPHERE is an instrument designed and built by a consortium consisting of IPAG (Grenoble, France), MPIA (Heidelberg, Germany), LAM (Marseille, France), LESIA (Paris, France), Laboratoire Lagrange (Nice, France), INAF – Osservatorio di Padova (Italy), Observatoire de Genève (Switzerland), ETH Zurich (Switzerland), NOVA (Netherlands), ONERA (France), and ASTRON (Netherlands), in collaboration with ESO. SPHERE was funded by ESO, with additional contributions from the CNRS (France), MPIA (Germany), INAF (Italy), FINES (Switzerland), and NOVA (Netherlands). SPHERE also received funding from the European Commission Sixth and Seventh Framework Programs as part of the Optical Infrared Coordination Network for Astronomy (OPTICON) under grant number RII3-Ct-2004-001566 for FP6 (2004–2008), grant number 226604 for FP7 (2009–2012), and grant number 312430 for FP7 (2013–2016).

## References

Allard, F., Homeier, D., & Freytag, B. 2012, Roy. Soc. Lond. Phil. Trans. Ser. A, 370, 2765
Allende Prieto, C., & Lambert, D. L. 1999, A&A, 352, 555
Allers, K. N., & Liu, M. C. 2013, ApJ, 772, 79
Amara, A., & Quanz, S. P. 2012, MNRAS, 427, 948

[13] We do not consider the combined ADI and dual-band imaging detection limits also reported in this paper (see note 12).

Ammons, S. M., Robinson, S. E., Strader, J., et al. 2006, ApJ, 638, 1004
Antichi, J., Dohlen, K., Gratton, R. G., et al. 2009, ApJ, 695, 1042
Ardila, D., Martín, E., & Basri, G. 2000, AJ, 120, 479
Bailer-Jones, C. A. L. 2011, MNRAS, 411, 435
Bailey, V., Meshkat, T., Reiter, M., et al. 2014, ApJ, 780, L4
Balona, L. A. 1987, SAAO Circular, 11, 1
Baraffe, I., Chabrier, G., Allard, F., & Hauschildt, P. H. 1998, A&A, 337, 403
Baraffe, I., Homeier, D., Allard, F., & Chabrier, G. 2015, A&A, 577, A42
Barber, R. J., Tennyson, J., Harris, G. J., & Tolchenov, R. N. 2006, MNRAS, 368, 1087
Barman, T. S., Macintosh, B., Konopacky, Q. M., & Marois, C. 2011, ApJ, 733, 65
Barnes, J. R., Collier Cameron, A., James, D. J., & Donati, J.-F. 2000, MNRAS, 314, 162
Bate, M. R. 2009, MNRAS, 392, 590
Bellini, A., Anderson, J., van der Marel, R. P., et al. 2014, ApJ, 797, 115
Beust, H., Bonnefoy, M., Maire, A.-L., et al. 2016, A&A, in press, DOI: 10.1051/0004-6361/201527388
Beuzit, J.-L., Feldt, M., Dohlen, K., et al. 2008, in SPIE Conf. Ser. 7014, eds. I. S. McLean, & M. M. Casali, 701418
Biller, B. A., Liu, M. C., Wahhaj, Z., et al. 2010, ApJ, 720, L82
Biller, B. A., Liu, M. C., Wahhaj, Z., et al. 2013, ApJ, 777, 160
Binks, A. S., & Jeffries, R. D. 2014, MNRAS, 438, L11
Boccaletti, A., Abe, L., Baudrand, J., et al. 2008, in SPIE Conf. Ser., 7015, 70151B
Bonnefoy, M., Lagrange, A.-M., Boccaletti, A., et al. 2011, A&A, 528, L15
Bonnefoy, M., Chauvin, G., Lagrange, A.-M., et al. 2014a, A&A, 562, A127
Bonnefoy, M., Currie, T., Marleau, G.-D., et al. 2014b, A&A, 562, A111
Bonnet, H., Abuter, R., Baker, A., et al. 2004, The Messenger, 117, 17
Boss, A. P. 1997, Science, 276, 1836
Bowler, B. P., Liu, M. C., Shkolnik, E. L., & Dupuy, T. J. 2013, ApJ, 774, 55
Brandt, T. D., McElwain, M. W., Turner, E. L., et al. 2014, ApJ, 794, 159
Brott, I., & Hauschildt, P. H. 2005, in The Three-Dimensional Universe with Gaia, ESA SP, 576, 565
Burgasser, A. J. 2014, in Astron. Soc. India Conf. Ser., 11, 7
Burgasser, A. J., McElwain, M. W., Kirkpatrick, J. D., et al. 2004, AJ, 127, 2856
Carson, J., Thalmann, C., Janson, M., et al. 2013, ApJ, 763, L32
Castelli, F., & Kurucz, R. L. 1994, A&A, 281, 817
Chauvin, G., Lagrange, A.-M., Dumas, C., et al. 2005a, A&A, 438, L25
Chauvin, G., Lagrange, A.-M., Zuckerman, B., et al. 2005b, A&A, 438, L29
Chauvin, G., Lagrange, A.-M., Bonavita, M., et al. 2010, A&A, 509, A52
Chauvin, G., Vigan, A., Bonnefoy, M., et al. 2015, A&A, 573, A127
Chilcote, J., Barman, T., Fitzgerald, M. P., et al. 2015, ApJ, 798, L3
Chincarini, G., Zerbi, F., Antonelli, A., et al. 2003, The Messenger, 113, 40
Claudi, R. U., Turatto, M., Gratton, R. G., et al. 2008, in SPIE Conf. Ser., 7014, 70143E
Close, L. M., Siegler, N., Freed, M., & Biller, B. 2003, ApJ, 587, 407
Close, L. M., Thatte, N., Nielsen, E. L., et al. 2007, ApJ, 665, 736
Coates, D. W., Halprin, L., Sartori, P., & Thompson, K. 1980, IBVS, 1849, 1
Coates, D. W., Innis, J. L., Moon, T. T., & Thompson, K. 1982, IBVS, 2248, 1
Cushing, M. C., Rayner, J. T., & Vacca, W. D. 2005, ApJ, 623, 1115
Cushing, M. C., Marley, M. S., Saumon, D., et al. 2008, ApJ, 678, 1372
Cutispoto, G. 1998, A&AS, 127, 207
Cutispoto, G., & Leto, G. 1997, A&AS, 121, 369
Cutispoto, G., Pastori, L., Pasquini, L., et al. 2002, A&A, 384, 491
Cutri, R. M., Skrutskie, M. F., van Dyk, S., et al. 2003, 2MASS All Sky Catalog of point sources
Cutri, R. M., et al. 2013, VizieR Online Data Catalog: II/328
Davies, R. I. 2007, MNRAS, 375, 1099
Dawson, P., Scholz, A., Ray, T. P., et al. 2014, MNRAS, 442, 1586
de la Reza, R., & Pinzón, G. 2004, AJ, 128, 1812
Devillard, N. 1997, The Messenger, 87, 19
Dohlen, K., Langlois, M., Saisse, M., et al. 2008, in SPIE Conf. Ser., 7014, 70143L
Ehrenreich, D., Lagrange, A.-M., Montagnier, G., et al. 2010, A&A, 523, A73
Eisenhauer, F., Abuter, R., Bickert, K., et al. 2003, in SPIE Conf. Ser. 4841, eds. M. Iye, & A. F. M. Moorwood, 1548
ESA 1997, The HIPPARCOS and TYCHO catalogues. Astrometric and photometric star catalogues derived from the ESA HIPPARCOS Space Astrometry Mission, ESA SP, 1200
Fusco, T., Rousset, G., Sauvage, J.-F., et al. 2006, Opt. Express, 14, 7515
Fusco, T., Sauvage, J.-F., Petit, C., et al. 2014, in SPIE Conf. Ser., 9148, 91481
Galicher, R., & Marois, C. 2011, in Proc. AO4ELT2, P25
Ginski, C., Neuhäuser, R., Mugrauer, M., Schmidt, T. O. B., & Adam, C. 2013, MNRAS, 434, 671
Ginski, C., Schmidt, T. O. B., Mugrauer, M., et al. 2014, MNRAS, 444, 2280
Gizis, J. E. 2002, ApJ, 575, 484
Gizis, J. E., Monet, D. G., Reid, I. N., et al. 2000, AJ, 120, 1085
Golimowski, D. A., Henry, T. J., Krist, J. E., et al. 2004, AJ, 128, 1733
Helling, C., Ackerman, A., Allard, F., et al. 2008, MNRAS, 391, 1854
Hinkley, S., Bowler, B. P., Vigan, A., et al. 2015a, ApJ, 805, L10
Hinkley, S., Kraus, A. L., Ireland, M. J., et al. 2015b, ApJ, 806, L9
Hugot, E., Ferrari, M., El Hadi, K., et al. 2012, A&A, 538, A139
Innis, J. L., Coates, D. W., Moon, T. T., & Thompson, K. 1983, IBVS, 2378, 1
Innis, J. L., Coates, D. W., & Thompson, K. 1988, MNRAS, 233, 887
Innis, J. L., Coates, D. W., Thompson, K., & Lloyd Evans, T. 1990, MNRAS, 242, 306
Innis, J. L., Coates, D. W., & Kaye, T. G. 2007, Peremennye Zvezdy, 27, 1
Itoh, Y., Hayashi, M., Tamura, M., et al. 2005, ApJ, 620, 984
Jenkins, J. S., Pavlenko, Y. V., Ivanyuk, O., et al. 2012, MNRAS, 420, 3587
Jones, A., Noll, S., Kausch, W., Szyszka, C., & Kimeswenger, S. 2013, A&A, 560, A91
Kharchenko, N. V. 2001, Kinematika i Fizika Nebesnykh Tel, 17, 409
Kiraga, M. 2012, Acta Astron., 62, 67
Kuzuhara, M., Tamura, M., Kudo, T., et al. 2013, ApJ, 774, 11
Lafrenière, D., Doyon, R., Marois, C., et al. 2007, ApJ, 670, 1367
Lafrenière, D., Jayawardhana, R., & van Kerkwijk, M. H. 2008, ApJ, 689, L153
Lafrenière, D., Jayawardhana, R., & van Kerkwijk, M. H. 2010, ApJ, 719, 497
Lagrange, A.-M., Bonnefoy, M., Chauvin, G., et al. 2010, Science, 329, 57
Lagrange, A.-M., Meunier, N., Chauvin, G., et al. 2013, A&A, 559, A83
Laher, R. R., Gorjian, V., Rebull, L. M., et al. 2012, PASP, 124, 737
Lenzen, R., Hartung, M., Brandner, W., et al. 2003, in SPIE Conf. Ser., eds. M. Iye, & A. F. M. Moorwood, 4841, 944
Liu, M. C., Dupuy, T. J., & Leggett, S. K. 2010a, ApJ, 722, 311
Liu, M. C., Wahhaj, Z., Biller, B. A., et al. 2010b, in SPIE Conf. Ser. 7736, eds. B. L. Ellerbroek, M. Hart, N. Hubin, & P. L. Wizinowich, 77361
Lloyd Evans, T., & Koen, M. C. J. 1987, SAAO Circular, 11, 21
Lodieu, N., Hambly, N. C., Jameson, R. F., & Hodgkin, S. T. 2008, MNRAS, 383, 1385
Looper, D. L., Burgasser, A. J., Kirkpatrick, J. D., & Swift, B. J. 2007, ApJ, 669, L97
Luhman, K. L., Stauffer, J. R., Muench, A. A., et al. 2003, ApJ, 593, 1093
Luhman, K. L., Wilson, J. C., Brandner, W., et al. 2006, ApJ, 649, 894
Luhman, K. L., Patten, B. M., Marengo, M., et al. 2007, ApJ, 654, 570
Lyot, B. 1932, Z. Astrophys., 5, 73
Macintosh, B., Graham, J. R., Ingraham, P., et al. 2014, PNAS, 111, 12661
Maire, A.-L., Boccaletti, A., Rameau, J., et al. 2014, A&A, 566, A126
Malo, L., Doyon, R., Feiden, G. A., et al. 2014, ApJ, 792, 37
Mamajek, E. E., & Bell, C. P. M. 2014, MNRAS, 445, 2169
Marley, M. S., Fortney, J. J., Hubickyj, O., Bodenheimer, P., & Lissauer, J. J. 2007, ApJ, 655, 541
Marois, C., Lafrenière, D., Doyon, R., Macintosh, B., & Nadeau, D. 2006a, ApJ, 641, 556
Marois, C., Lafrenière, D., Macintosh, B., & Doyon, R. 2006b, ApJ, 647, 612
Marois, C., Macintosh, B., Barman, T., et al. 2008, Science, 322, 1348
Marois, C., Macintosh, B., & Véran, J.-P. 2010a, in SPIE Conf. Ser. 7736, eds. B. L. Ellerbroek, M. Hart, N. Hubin, & P. L. Wizinowich, 77361J
Marois, C., Zuckerman, B., Konopacky, Q., Macintosh, B., & Barman, T. 2010b, Nature, 468, 1080
Marois, C., Correia, C., Galicher, R., et al. 2014, in SPIE Conf. Ser., 9148, 91480
Masciadri, E., Mundt, R., Henning, T., Alvarez, C., & Barrado y Navascués, D. 2005, ApJ, 625, 1004
McLean, I. S., McGovern, M. R., Burgasser, A. J., et al. 2003, ApJ, 596, 561
Mentuch, E., Brandeker, A., van Kerkwijk, M. H., Jayawardhana, R., & Hauschildt, P. H. 2008, ApJ, 689, 1127
Mesa, D., Gratton, R., Zurlo, A., et al. 2015, A&A, 576, A121
Meshkat, T., Kenworthy, M. A., Reggiani, M., et al. 2015, MNRAS, 453, 2533
Messina, S., Desidera, S., Turatto, M., Lanzafame, A. C., & Guinan, E. F. 2010, A&A, 520, A15
Metchev, S. A., & Hillenbrand, L. A. 2006, ApJ, 651, 1166
Modigliani, A., Hummel, W., Abuter, R., et al. 2007, ArXiv e-prints [arXiv:astro-ph/0701297]
Mugrauer, M., Vogt, N., Neuhäuser, R., & Schmidt, T. O. B. 2010, A&A, 523, L1
Mugrauer, M., Röll, T., Ginski, C., et al. 2012, MNRAS, 424, 1714
Murphy, S. J., & Lawson, W. A. 2015, MNRAS, 447, 1267
Nielsen, E. L., Liu, M. C., Wahhaj, Z., et al. 2012, ApJ, 750, 53
Nielsen, E. L., Liu, M. C., Wahhaj, Z., et al. 2013, ApJ, 776, 4
Noll, S., Kausch, W., Barden, M., et al. 2012, A&A, 543, A92
Pavlov, A., Möller-Nilsson, O., Feldt, M., et al. 2008, in SPIE Conf. Ser., 7019, 701939
Pearce, T. D., Wyatt, M. C., & Kennedy, G. M. 2014, MNRAS, 437, 2686
Pecaut, M. J., & Mamajek, E. E. 2013, ApJS, 208, 9
Perrin, M. D., Maire, J., Ingraham, P., et al. 2014, in SPIE Conf. Ser., 9147, 3
Petit, C., Sauvage, J.-F., Fusco, T., et al. 2014, in SPIE Conf. Ser., 9148, 91480

Pojmanski, G. 1997, Acta Astron., 47, 467
Pollack, J. B., Hubickyj, O., Bodenheimer, P., et al. 1996, Icarus, 124, 62
Racine, R., Walker, G. A. H., Nadeau, D., Doyon, R., & Marois, C. 1999, PASP, 111, 587
Raghavan, D., McAlister, H. A., Henry, T. J., et al. 2010, ApJS, 190, 1
Rameau, J., Chauvin, G., Lagrange, A.-M., et al. 2013a, ApJ, 772, L15
Rameau, J., Chauvin, G., Lagrange, A.-M., et al. 2013b, A&A, 553, A60
Randich, S., Gratton, R., & Pallavicini, R. 1993, A&A, 273, 194
Rayner, J. T., Toomey, D. W., Onaka, P. M., et al. 2003, PASP, 115, 362
Rayner, J. T., Cushing, M. C., & Vacca, W. D. 2009, ApJS, 185, 289
Rebull, L. M., Stapelfeldt, K. R., Werner, M. W., et al. 2008, ApJ, 681, 1484
Riviere-Marichalar, P., Barrado, D., Montesinos, B., et al. 2014, A&A, 565, A68
Roberts, D. H., Lehar, J., & Dreher, J. W. 1987, AJ, 93, 968
Rossow, W. B. 1978, Icarus, 36, 1
Rousset, G., Lacombe, F., Puget, P., et al. 2003, in SPIE Conf. Ser. 4839, eds. P. L. Wizinowich & D. Bonaccini, 140
Sauvage, J.-F., Fusco, T., Petit, C., et al. 2014, in SPIE Conf. Ser., 9148, 914847
Scargle, J. D. 1982, ApJ, 263, 835
Schmidt, T. O. B., Mugrauer, M., Neuhäuser, R., et al. 2014, A&A, 566, A85
Scholz, A., Coffey, J., Brandeker, A., & Jayawardhana, R. 2007, ApJ, 662, 1254
Siess, L., Dufour, E., & Forestini, M. 2000, A&A, 358, 593
Sivaramakrishnan, A., & Oppenheimer, B. R. 2006, ApJ, 647, 620
Soderblom, D. R., King, J. R., & Henry, T. J. 1998, AJ, 116, 396
Soubiran, C., Le Campion, J.-F., Cayrel de Strobel, G., & Caillo, A. 2010, A&A, 515, A111
Soummer, R. 2005, ApJ, 618, 161
Soummer, R., Pueyo, L., & Larkin, J. 2012, ApJ, 755, L28
Sparks, W. B., & Ford, H. C. 2002, ApJ, 578, 543
Spiegel, D. S., & Burrows, A. 2012, ApJ, 745, 174
Stetson, P. B. 1987, PASP, 99, 191
Thalmann, C., Schmid, H. M., Boccaletti, A., et al. 2008, in SPIE Conf. Ser., 7014, 70143
Thalmann, C., Carson, J., Janson, M., et al. 2009, ApJ, 707, L123
Torres, C. A. O., Quast, G. R., da Silva, L., et al. 2006, A&A, 460, 695
Torres, C. A. O., Quast, G. R., Melo, C. H. F., & Sterzik, M. F. 2008, in Handbook of Star Forming Regions, II, ASP Monograph Publications, 5, ed. B. Reipurth, 757
van Biesbroeck, G. 1961, AJ, 66, 528
van der Bliek, N. S., Manfroid, J., & Bouchet, P. 1996, A&AS, 119, 547
van Leeuwen, F. 2007, A&A, 474, 653
Vigan, A., Langlois, M., Moutou, C., & Dohlen, K. 2008, A&A, 489, 1345
Vigan, A., Moutou, C., Langlois, M., et al. 2010, MNRAS, 407, 71
Vigan, A., Bonnefoy, M., Chauvin, G., Moutou, C., & Montagnier, G. 2012a, A&A, 540, A131
Vigan, A., Patience, J., Marois, C., et al. 2012b, A&A, 544, A9
Vigan, A., Bonnefoy, M., Ginski, C., et al. 2016, A&A, 587, A55
Wahhaj, Z., Liu, M. C., Biller, B. A., et al. 2011, ApJ, 729, 139
Wahhaj, Z., Liu, M. C., Nielsen, E. L., et al. 2013, ApJ, 773, 179
Zimmerman, N., Brenner, D., Oppenheimer, B. R., et al. 2011, PASP, 123, 746
Zuckerman, B., Song, I., Bessell, M. S., & Webb, R. A. 2001, ApJ, 562, L87
Zuckerman, B., Vican, L., Song, I., & Schneider, A. 2013, ApJ, 778, 5

[1] INAF−Osservatorio Astronomico di Padova, Vicolo dell'Osservatorio 5, 35122 Padova, Italy
e-mail: annelise.maire@oapd.inaf.it
[2] Université Grenoble Alpes, IPAG, 38000 Grenoble, France
e-mail: mickael.bonnefoy@obs.ujf-grenoble.fr
[3] CNRS, IPAG, 38000 Grenoble, France
[4] Leiden Observatory, Leiden University, PO Box 9513, 2300 RA Leiden, The Netherlands
e-mail: ginski@strw.leidenuniv.nl
[5] Aix Marseille Université, CNRS, LAM (Laboratoire d'Astrophysique de Marseille) UMR 7326, 13388 Marseille, France
e-mail: arthur.vigan@lam.fr
[6] European Southern Observatory, Alonso de Cordova 3107, Casilla 19001 Vitacura, Santiago 19, Chile
[7] INAF Catania Astrophysical Observatory, via S. Sofia 78, 95123 Catania, Italy
e-mail: sergio.messina@oact.inaf.it
[8] LESIA, CNRS, Observatoire de Paris, Université Paris Diderot, UPMC, 5 place J. Janssen, 92190 Meudon, France
[9] Max-Planck-Institut für Astronomie, Königstuhl 17, 69117 Heidelberg, Germany
[10] International Max Planck Research School for Astronomy and Space Physics, 69117 Heidelberg, Germany
[11] York Creek Observatory, Georgetown, Tasmania, Australia
[12] Institute for Astronomy, ETH Zurich, Wolfgang-Pauli-Strasse 27, 8093 Zurich, Switzerland
[13] Geneva Observatory, University of Geneva, Chemin des Maillettes 51, 1290 Versoix, Switzerland
[14] Núcleo de Astronomía, Facultad de Ingeniería, Universidad Diego Portales, Av. Ejercito 441, Santiago, Chile
[15] Millennium Nucleus "Protoplanetary Disk", Departamento de Astronomía, Universidad de Chile, Casilla 36-D, Santiago, Chile
[16] INAF−Osservatorio Astrofisico di Arcetri, largo E. Fermi 5, 50125 Firenze, Italy
[17] INAF−Osservatorio Astronomico di Capodimonte, Salita Moiariello 16, 80131 Napoli, Italy
[18] Anton Pannekoek Astronomical Institute, University of Amsterdam, PO Box 94249, 1090 GE Amsterdam, The Netherlands
[19] ONERA, The French Aerospace Lab BP72, 29 avenue de la Division Leclerc, 92322 Châtillon Cedex, France
[20] Kiepenheuer-Institut für Sonnenphysik, Schöneckstr. 6, 79104 Freiburg, Germany
[21] European Southern Observatory, Karl Schwarzschild St, 2, 85748 Garching, Germany
[22] Centre de Recherche Astrophysique de Lyon, CNRS/ENS-L/Université Lyon 1, 9 av. Ch. André, 69561 Saint-Genis-Laval, France
[23] Laboratoire Lagrange, UMR 7293, Observatoire de la Côte d'Azur (OCA), Université de Nice-Sophia Antipolis (UNS), CNRS, Bd. de l'Observatoire, 06304 Nice, France
[24] Department of Astronomy, California Institute of Technology, 1200 E. California Blvd, MC 249-17, Pasadena, CA 91125, USA
[25] CNRS, Canada-France-Hawaii Telescope Corporation, 65-1238 Mamalahoa Hwy., Kamuela, HI-96743, USA
[26] NOVA Optical-Infrared Instrumentation Group at ASTRON, Oude Hoogeveensedijk 4, 7991 PD Dwingeloo, The Netherlands